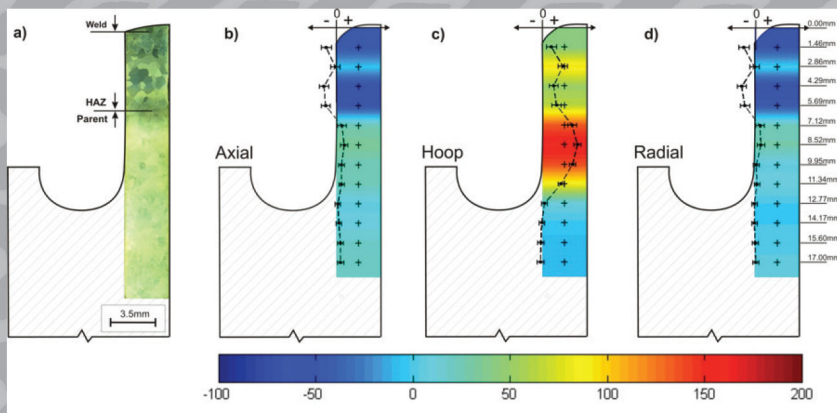


# International Conference on Residual Stresses 2016 ICRS-10



Edited by  
Thomas M. Holden  
Ondrej Muránsky  
Lyndon Edwards

**Residual Stresses 2016**  
ICRS-10

Edited by

Thomas M. Holden  
Ondrej Muránsky  
Lyndon Edwards

This book presents the proceedings of the Tenth International Conference on Residual Stresses which was devoted to the prediction/modelling, evaluation, control, and application of residual stresses over a wide range of applications. New developments on stress-measurement techniques, on the modelling and prediction of residual stresses and on progress made in the fundamental understanding of the nature of residual stresses are highlighted. The proceedings offer an overview of the current understanding of how residual stresses affect the properties of materials, components and structures.



# **Residual Stresses 2016**

## **ICRS-10**

10th International Conference on Residual Stresses  
(ICRS10), Sydney, Australia, 3-7 July, 2016.

**Thomas M. Holden, Ondrej Muránsky,  
Lyndon Edwards**

Institute of Materials Engineering Australian Nuclear Science &  
Technology Organization, Locked Bag 2001, Kirrawee DC,  
Sydney NSW 2232, Australia

### Peer review statement

All papers published in this volume of “Materials Research Proceedings” have been peer reviewed. The process of peer review was initiated and overseen by the above proceedings editors. All reviews were conducted by expert referees in accordance to Materials Research Forum LLC high standards.

Copyright © 2017 by authors

 Content from this work may be used under the terms of the Creative Commons Attribution 3.0 license. Any further distribution of this work must maintain attribution to the author(s) and the title of the work, journal citation and DOI.

Published under License by **Materials Research Forum LLC**  
Millersville, PA 17551, USA

Published as part of the proceedings series  
**Materials Research Proceedings**  
Volume 2 (2017)

ISSN 2474-3941 (Print)  
ISSN 2474-395X (Online)

ISBN 978-1-94529116-6 (Print)  
ISBN 978-1-94529117-3 (eBook)

This book contains information obtained from authentic and highly regarded sources. Reasonable efforts have been made to publish reliable data and information, but the author and publisher cannot assume responsibility for the validity of all materials or the consequences of their use. The authors and publishers have attempted to trace the copyright holders of all material reproduced in this publication and apologize to copyright holders if permission to publish in this form has not been obtained. If any copyright material has not been acknowledged please write and let us know so we may rectify in any future reprint.

Distributed worldwide by

**Materials Research Forum LLC**  
105 Springdale Lane  
Millersville, PA 17551  
USA  
<http://www.mrforum.com>

Manufactured in the United State of America  
10 9 8 7 6 5 4 3 2 1

# Table of Contents

*Preface*

*Committees*

<b>Numerical Investigation of Residual Stresses in Chain-die Formed AHSS U-Channels</b> Y. Sun, Z. Qian, V. Luzin, W.J.T Daniel, M. Zhang, S. Ding .....	1
<b>Quasi-static Process Modelling of Deep Cold Rolling on Ti-6Al-4V</b> A. Lim, S. Castagne, C.C. Wong .....	7
<b>Effect of Cooling and Shot Peening on Residual Stresses and Fatigue Performance of Milled Inconel 718</b> Z. Chen, R.L. Peng, J. Moverare, O. Widman, D. Gustafsson, S. Johansson .....	13
<b>Effect of Ultrasonic Peening on Residual Stresses at a T-Butt Weld Toe</b> A.K. Hellier, B.G. Prusty, G.M. Pearce, M. Reid, A.M. Paradowska, P. Simons .....	19
<b>Structural Engineering Studies on Reinforced Concrete Structure using Neutron Diffraction</b> H. Suzuki, K. Kusunoki, M. Kanematsu, T. Mukai, S. Harjo .....	25
<b>Stress Analysis of the Bi-Metallic Coins – a Potential Shrink Fit Ring &amp; Plug Standard</b> S. Olsen, V. Luzin .....	31
<b>Residual Stress Measurements Inside a Small Inner Diameter Hole at Low Bragg Angle Using X-Ray Diffraction Technique</b> M. Belassel, J. Pineault, M. Brauss .....	37
<b>Comparison of Residual Stress Measurement Techniques and Implementation Using X-Ray Diffraction</b> M. Belassel, J. Pineault, N. Caratanasov, M. Brauss .....	43
<b>Residual Stress Field Prediction in Shot Peened Mechanical Parts with Complex Geometries</b> M. Gelineau, L. Barrallier, E. Rouhaud, R. Kubler, Q. Puydt .....	49
<b>Comparison of Two X-Ray Residual Stress Measurement Methods: <math>\sin^2 \psi</math> and <math>\cos \alpha</math>, Through the Determination of a Martensitic Steel X-Ray Elastic</b> D. Delbergue, D. Texier, M. Lévesque, P. Bocher .....	55
<b>Residual Stress Measurement of Ti-Metal Samples by Means of XRD with Ti and Cu Radiation</b> L. Suominen, T. Rickert, S. Send .....	61
<b>Residual Stresses in Uniaxial Cyclic Loaded Pearlitic Lamellar Graphite Iron</b> M. Lundberg, J. Saarimäki, R.L. Peng, J.J. Moverare .....	67
<b>3D Residual Stresses in Selective Laser Melted Hastelloy X</b> J. Saarimäki, M. Lundberg, J.J. Moverare, H. Brodin .....	73
<b>Numerical Simulation of Residual Stresses Induced by Weld Repair in a Stainless Steel Pipe Considering the Influence of an Initial Fabrication Weld</b> G. Salerno, C. Bennett, W. Sun, A.A. Becker .....	79

<b>Analysis of Residual Stress Relaxation Under Mechanical Cyclic Loading of Shot-Peened TRIP780 Steel</b>	
C. Mauduit, R. Kubler, L. Barrallier, S. Berveiller, Q. Puydt, M. Monin, B. Weber .....	85
<b>Validation of XRD Stress Analyses Combining in-situ Tests and Integrated Peak Processing</b>	
B. Voillot, R. Billardon, J.L. Lebrun, F. Hild.....	91
<b>Residual Stresses in Modelling Fatigue Lifetime of Gas Nitrided Iron-Based Alloys</b>	
H. Weil, L. Barrallier, S. Jégou, A. Courleux, G. Beck .....	97
<b>Comparison of X-Ray Residual Stress Measurement Values by Cos <math>\alpha</math> Method and Sin<sup>2</sup> <math>\Psi</math> Method</b>	
A. Kohri, Y. Takaku, M. Nakashiro.....	103
<b>Residual Stress Influence on the Flexural Buckling of Welded I-Girders</b>	
B. Launert, M. Rhode, A. Kromm, H. Pasternak, T. Kannengiesser .....	109
<b>Measurement of Highly Non-uniform Residual Stress Fields in Thin Plate Using a New Side Cut Destructive Method</b>	
H.K. Kima, M.J. Pavierb, A. Shterenlikhtc.....	115
<b>Evaluation of Residual Stress in the Hot Forming Process Using Hole Drilling</b>	
M.J. Azizpour, H. Fattahi .....	121
<b>Through Thickness Residual Stress and Microstructural Mapping of AA7085-T7452 Die Forging</b>	
P.S. Baburamani, K.F. Walker, P.K. Sharp , J. Niclis, A. Shekhter .....	127
<b>Validation of Neutron Diffraction and the Incremental Deep Hole Drilling Residual Stress Measurements of a High Strength T Butt Weld Test Piece Using the Contour Residual Stress Measurement Technique</b>	
G. Sloan, X. Ficquet, D. Cave, K. Serasli, E. Kingston, V. Linton .....	133
<b>Cementite Residual Stress Analysis in Gas-nitrided Low Alloy Steels</b>	
L. Barrallier, S. Goekjian, F. Guittonneau, S. Jégou .....	139
<b>Residual Stress Measurement in a High Strength T Butt Weld Specimen by the Neutron Diffraction and Deep Hole Drilling Techniques</b>	
G.W. Sloan, V.M. Linton, O. Kirstein, X. Ficquet, E. Kingston.....	145
<b>The Residual Stress Effect on the Shape Memory Polymers</b>	
A. Kallel, M. Lamraoui, J. Fitoussi, A. Tcharkhtchi .....	151
<b>Residual Stress Measurements of Alumina-Zirconia Ceramics by Time-of-Flight Neutron Diffraction</b>	
K. Fan, J. Ruiz-Hervias, J. Gurauskis, C. Baudin .....	157
<b>Combining Sectioning Method and X Ray Diffraction for Evaluation of Residual Stresses in Welded High Strength Steel Components</b>	
A. Kromm, M. Rhode, B. Launert, J. Dixneit, T. Kannengiesser, H. Pasternak.....	163
<b>Influence of Weld Repair by Gouging on the Residual Stresses in High Strength Steels</b>	
A. Kromm, R. Schasse, P. Xu, T. Mente, T. Kannengiesser .....	169

<b>Residual Stress States After Piezo Peening Treatment at Cryogenic and Elevated Temperatures Predicted by FEM Using Suitable Material Models</b>	
A. Klumpp, M. Tamam, F. Lienert, S. Dietrich, J. Gibmeier, V. Schulze .....	175
<b>Residual Stress Analysis in Injection Moulded Polycarbonate Samples</b>	
A. Magnier, B. Scholtes, T. Niendorf .....	181
<b>Local Residual Stress Analysis on Deep Drawn Cups by Means of the Incremental Hole-Drilling Method</b>	
S. Schuster, J. Pagenkopf, J. Gibmeier .....	187
<b>Bending Fatigue Behavior of Blast Cleaned Grey Cast Iron</b>	
M. Ahmad, R.L. Peng, M. König, S. Johansson .....	193
<b>Elastic and Elastic-Plastic Behaviour of a Crack in a Residual Stress Field</b>	
G. Wua, C. Airdb, D. Smith, M. Pavierc .....	199
<b>Multi-axial Analyses of Welding Stresses in High-Strength Steel Welds</b>	
D. Schroepfer, K. Flohr, A. Kromm, T. Kannengiesser .....	205
<b>Evaluation of Residual Stress by X-Ray Diffraction and Correlative Stress Modelling</b>	
S. Kumar, A. Crivoi, M.J. Tan, A. Tai, I. Marinescu .....	211
<b>The Relationship between X-Ray Stress Measured Value and Applied Stress in Elastic/Plastic Deformation Region in Tensile Testing</b>	
M. Nakashiro, Y. Takaku, Y. Mitani, A. Kohri .....	216
<b>Influence of Heat Control on Residual Stresses in Low Transformation Temperature (LTT) Large Scale Welds</b>	
J. Dixneit, A. Kromm, M. Boin, T. Kannengiesser, J. Gibmeier .....	223
<b>Residual Stress Analysis in Girth-welded Ferritic and Austenitic Steel Pipes Using Neutron and X-Ray Diffraction</b>	
N. Hempel, J.R. Bunn, T. Nitschke-Pagel, E.A. Payzant, K. Dilger .....	229
<b>Effect of Plasticity on Residual Stresses Obtained by the Incremental Hole-drilling Method with 3D FEM Modelling</b>	
E. Van Puymbroeck, W. Nagy, H. De Backer .....	235
<b>Ultrasonic Non-destructive Testing and in Situ Regulation of Residual Stress</b>	
C. Xu, H. Tian, W. Song, J. Song .....	241
<b>Residual Stress and Contact Force Study for Deep Cold Rolling of Aero-engine Material</b>	
A. Prithiviraja, W. Weib .....	247
<b>Influence of the Pre-Stressing on the Residual Stresses Induced by Deep Rolling</b>	
N. Lyubenova, M. Jacquemin, D. Bähre .....	253
<b>Measurements of Surface and Near-surface Residual Stress in 4330 Low Alloy Carbon Steel Weld Clad Components</b>	
G. Benghalia, S. Rahimi, J. Wood .....	259
<b>Accuracy and Stability of 2D-XRD for Residual Stress Measurement</b>	
B.B. He .....	265

<b>Turning Residual Stresses in Functionally Graded Steel Components</b>	
W. Zinn, M. Tiffe, D. Biermann, B. Scholtes.....	271
<b>Residual Stress Condition of Tubular Laser Welds of an AZ31 Magnesium Alloy</b>	
T. Nitschke-Pagel, K. Dilger.....	277
<b>Effects of Hydrostatic 2<sup>nd</sup> Kind Residual Stresses and of Carbon Partitioning During Martensitic Quenching of Low Alloy Steel</b>	
J. Epp.....	283
<b>Residual Stress in Stainless Steels after Surface Grinding and its Effect on Chloride Induced SCC</b>	
N. Zhou, R.L. Peng, R. Pettersson, M. Schönning.....	289
<b>How Precise can be the Residual Stress Determined by X-Ray Diffraction? A summary of the Possibilities and Limits</b>	
E. Mueller .....	295
<b>Challenges in the Calculation of Residual Stresses in Thick-walled Components</b>	
J. Klassen, T. Nitschke-Pagel, K. Dilger .....	299
<b>Residual Stress Relaxation in Welded Steel Joints – an Experimentally-based Model</b>	
J. Hensel, T. Nitschke-Pagel, K. Dilger.....	305
<b>Investigations of the Residual Stresses and Surface Integrity Generated by a Novel Mechanical Surface Strengthening</b>	
D.T. Ardi, W. Wei, I. Parr, G. Feldmann, A. Aramcharoen, C.C. Wong .....	311
<b>Evaluation of Thickness and Residual Stress of Shallow Surface Regions from Diffraction Profiles</b>	
W. Pfeiffera, E. Reisacher .....	317
<b>Evaluation of Residual Stress Determinations Conducted with Laser Ablation and Optical Displacement Measurement</b>	
P. Weidmann, G. Pedrini, V. Martínez-García <sup>3</sup> , M. Wenzelburger, A. Killinger, S. Schmauder, R. Gadow, W. Osten.....	323
<b>Evaluation of the Three-dimensional Welding Residual Stresses Based on the Eigenstran Methodology via X-Ray Measurements</b>	
M. Ogawa, T. Ishii .....	329
<b>X-Ray Diffraction Measurements and Investigation of the Stress Relaxation in Autofrettaged AISI 4140 Steel Thick Walled Cylinders</b>	
N. Lyubenova, J. Pineault, H. Brünnet, D. Bähre .....	335
<b>Contour, iDHD, and ICHD Residual Stress Measurements on a T-Section Plate</b>	
X. Ficquet, D. Douglas, K. Serasli, F. Bridier .....	341
<b>Characterisation of the Effect of Corrosion on the Residual Stresses in Girth Weld Pipe Using Ultrasonic Calibrated with Strain-relieving Measurement Techniques</b>	
R. Romac, D. Cave, X. Ficquet .....	347
<b>The Effects of Residual Stress on Elastic-Plastic Fracture: Two Diffraction Studies</b>	
H. Coules, G. Horne, M. Peel .....	353

<b>Residual Stress Study of Al/Al Laminates Processed by Accumulative Roll Bonding</b>	
L. Su, C. Lu, H. Li, V. Luzin, H. Wang, K. Tieu.....	359
<b>Residual Stress Analysis on Oxide Layers Obtained by High Temperature Oxidation of Chromia-Forming Alloys</b>	
N. Li, J. Xiao, N. Prud'homme, L. Li, V. Ji.....	365
<b>Neutron Optics Upgrades to the Residual Stress Diffractometer, KOWARI</b>	
M. Reid, S. Olsen, V. Luzin, M. New, N. Booth, D. Clowes, T. Nguyen, F. Franceschini, A. Ogrin, S. Pangalis, A. Paradowska, N. Larkin, Z. Pan, N. Hoye, H. Suzuki.....	371
<b>Extension of the Deep-Hole Drilling Method for the Measurement of in-Plane Residual Stresses in Composite Laminates</b>	
C. Garza, R. Das, M.J. Pavier, A. Shterenlikht, D.J. Smith.....	377
<b>Residual Stresses in Selective Laser Melted Components of Different Geometries</b>	
M. Reid, T. Sercombe, A. Paradowska, X. Li .....	383
<b>Residual Stresses Determination with Plasticity Effects by Electron Speckle-Interferometry Hole-Drilling Method</b>	
L. Lobanov, V. Savitsky.....	389
<b>Numerical Modelling and Mitigation Technique of Welding Distortion for Fillet Welding of Aluminum Plate</b>	
M. Tsunori, M. Mouri, S. Saso, H. Kusumoto.....	395
<b>Residual Stress in Metal-Matrix Composite Cylinder Measured by Neutron Diffraction and Contour Method</b>	
V. Luzin, K. Thorogood, J.R. Griffiths, C.J. Davidson, T.R. Finlayson .....	401
<b>Simulative Investigations of the Influence of Surface Indentations on Residual Stresses on Inner Raceways for Roller Element Bearings</b>	
J. Kehl, R. Drafz, F. Pape, G. Poll .....	407
<b>Benchmarking studies of the MPISI Material Science Diffractometer at SAFARI-1</b>	
A.M. Venter, D. Marais, V. Luzin .....	413
<b>Discussing of Deformation of Additive Manufacturing due to External Bending</b>	
Y.J. Lin, J.C. Wang, C.Y. Su, C.H. Yang .....	419
<b>Residual Stresses in Dengeling-Treated Aluminum Alloy AA 7050</b>	
L. Selegård, R.L. Peng, A. Billenius, G. Petersén, M. ESS, M. Jonsson.....	425
<b>In situ X-Ray Diffraction Investigation of Surface Modifications in a Deep Rolling Process under Static Condition</b>	
H. Meyer, J. Epp, H.W. Zoch.....	431
<b>Analysis of the Residual Stress in ARMOX 500T Armour Steel and Numerical Study of the Resultant Ballistic Performance</b>	
M. Saleh, V. Luzin, M.M. Kariem, D. Ruan .....	437
<b>Structural Characterization of Ancient Japanese Swords from MAAS Using Neutron Strain Scanning Measurements</b>	
F. Salvemini, V. Luzin, F. Grazzi, S. Gatenby, M.J. Kim.....	443

<b>A Portable Optical DSPI System for Residual Stresses Measurement by Hole Drilling Using the Integral Method in Terms of Displacement</b>	
A.G. Albertazzi, M. Viotti, C. Veiga .....	449
<b>Residual Stress Characterization and Control in the Additive Manufacture of Large Scale Metal Structures</b>	
J.R. Hönnige, S. Williams, M.J. Roy, P. Colegrove, S. Ganguly .....	455
<b>Tensile Residual Stress Mitigation Using Low Temperature Phase Transformation Filler Wire in Welded Armor Plates</b>	
X. Yu, D. Tzelepis, J. Bunn, A.E. Payzant, Z. Feng.....	461
<b>In-situ Monitoring of Laser Surface Line Hardening by Means of Synchrotron X-Ray Diffraction</b>	
D. Kiefer, J. Gibmeier, F. Beckmann, F. Wilde.....	467
<b>Consideration of Tool Chamfer for Realistic Application of the Incremental Hole-Drilling Method</b>	
N. Simon, J. Gibmeier.....	473
<b>Full Stress Tensor Determination during Phase Transformation of a Metal Matrix Composite by in situ High Energy X-Ray Diffraction and Micromechanical Simulations</b>	
G. Geandier, L. Vautrot, B. Denand, M. Dehmas, E. Aeby-Gautiera, J. Teixeira, S. Denisa....	479
<b>In-vitro Investigation of Air Plasma-Sprayed Hydroxyapatite Coatings by Diffraction Techniques</b>	
T.P. Ntsoane, C. Theron, A. Venter, M. Topic, M. Härting, R. Heimann .....	485
<b>Residual Stress Behavior in Hardened Shot Peened 42CrMo4 Specimens during Fatigue Load</b>	
D. Cseh, V. Mertinger, J. Lukacs .....	491
<b>Stress in Thin Wall Structures Made by Layer Additive Manufacturing</b>	
V. Luzin, N. Hoye .....	497
<b>Effect of Element on Porosity and Residual Stress Distribution of A7N01S-T5 Aluminum Alloy Welded Joints in High-Speed Trains</b>	
Y. Liu, J. Chen, G. Guo, J. An, H. Chen.....	503
<b>Evaluation of Residual Stress Effects in Aft Pressure Ring Frame of a Royal Australian Air Force P-3C Maritime Patrol Aircraft</b>	
K. Walker, M. Ryan, J. Ayling.....	509
<b>A Non-Destructive Investigation of two Cypriot Bronze Age Knife Blades using Neutron Diffraction Residual Stress Analysis</b>	
C. Davey, D Saunders, V. Luzin, J. Bevitt, J. Webb, J. Donlon, M. Ionescu.....	515
<b>Study of Stress Partitioning in a 0.68 wt%C Pearlitic Steel Using High Energy X-Ray Synchrotron Radiation</b>	
C. Braham, A. Baczmański, G. Gonzalez, H. Sidhom, E. Gadalińska, S. Wroński, T. Buslaps, R. Wawszczak .....	521
<b>Effect of Thermal and Mechanical Loadings on the Residual Stress Field in a Nickel Based Superalloy using X-Ray Laue Microdiffraction</b>	
G. Altinkurt, M. Fèvre, G. Geandier, O. Robach, S. Guernaoui, M. Dehmas .....	527

<b>Comparison of Submerged Arc Welding Process Modification Influence on Thermal Strain by in-situ Neutron Diffraction</b>	
R. Sharma, U. Reisgen, M. Hofmann.....	533
<b>Residual Stresses on Electro-Deposited NiCo-Al and NiCo-Zr Composite Coatings</b>	
F. Cai, C. Jiang, B. Pan .....	539
<b>Neutron Diffraction Measurements of Residual Stress and Mechanical Testing of Pressure Sintered Metal-Ceramic Composite Systems</b>	
K. Toppler, V. Luzin, M. Saleh, A. Ruys, K. Kabir, D. Chavara .....	545
<b>The Role of Intergranular Stresses in Plastic Deformation Studied Using a Diffraction and Self-Consistent Model</b>	
E. Gadalińska, A. Baczmański, M. Wróbel, S. Wroński, M. Wroński, R. Wawszczak, C. Braham, Y. Zhao, L. Le Joncour, T. Buslaps, Ch. Scheffzük .....	551
<b>Experimental Investigation of Welding Stresses in MWIC Weldability Test</b>	
H. Alipooramirabad, A. Paradowska, R. Ghomashchi, N. Hoye, M. Reid .....	557
<b>Investigating the Effects of Mitigation Techniques on Residual Stress and Microstructure of HSLA Welds</b>	
H. Alipooramirabad, R. Ghomashchi, A. Paradowska, M. Reid .....	563
<b>Residual Stress Measurements in Vintage LPG Pressure Vessel Welds, via Neutron Diffraction</b>	
K. Sozen, A. Paradowska, M. Reid, R. Griffins, J. Daniels.....	569
<b>Challenges of Measuring Residual Stresses in Large Girth Welded Pipe Spools by Neutron Diffraction</b>	
Y. Ren, A. Paradowska, E. Eren, B. Wang .....	575
<b>Design and Manufacture of Industrially Representative Weld Mock-ups for the Quantification of Residual Stresses in a Nuclear Pressure Vessel Steel</b>	
J.A. Francis, M.C. Smith, B. Jeyaganesh, A.N. Vasileiou, D.W. Rathod, M.J. Roy, N.M. Irvine.....	581
<b>Effects of Numerical Methods on Residual Stress Evaluation by the Incremental Hole-Drilling Technique Using the Integral Method</b>	
B. Gore, J.P. Nobre.....	587
<b>Residual Stress Redistribution due to Removal of Material Layers by Electrolytic Polishing</b>	
I. Surtee, J.P. Nobre.....	593
<b>Research on Corrosion Fatigue Crack Propagation Behavior of Welded Joints of A7N01P-T4 Aluminum Alloys</b>	
J. Chen, J. Xu, M. Zhao, G. Gou .....	599
<b>Residual Stress and Critical Crack Size before and after Post-Weld Heat-Treatment</b>	
M. Law, A. Paradowska, N. Hoye, P. Grace.....	603
<b>Dislocation Density of GlidCop with Compressive Strain applied at High Temperature</b>	
M. Sano, S. Takahashi, A. Watanabe, A. Shiro, T. Shobu.....	609
<i>Keyword and Author Index</i> .....	615
<i>About the editors</i> .....	623

## Preface

ICRS-10, the 10th International Conference on Residual Stresses, was held at the Novotel Sydney Brighton Beach Hotel at Brighton Le Sands, Sydney between the 3<sup>rd</sup> and the 7<sup>th</sup> of July 2016.

ICRS-10 was the latest of a highly successful series which started in Garmisch-Partenkirchen (Germany) thirty years ago and continued in Nancy (France, 1988), Tokushima (Japan, 1991), Baltimore (USA, 1994), Linköping (Sweden, 1997), Oxford (UK, 2000), Xi'an (China, 2004) and Denver (USA, 2008) and, again in Garmisch-Partenkirchen (Germany, 2012).

The conference continues to be the key forum for scientists and engineers interested in the prediction, evaluation, control, and application of residual stresses. ICRS-10 featured 149 oral and 30 poster presentations given to 206 predominantly international attendees from 31 countries.

Publication in these proceedings was voluntary and after peer review a total of 102 papers are included in these proceedings. This could not have been achieved without the very significant efforts of both reviewers and authors. Without this work these proceedings could not exist and I would like to thank them on behalf of the community.

I hope that all those who attended would share my opinion that ICRS-10 was a vibrant, exciting and productive conference and that these proceedings give some sense of the success of ICRS-10 to the reader.

Finally, I would like to thank the members of both the ICRS Scientific Board the ICRS-10 Organizing Committee without whose tireless work ICRS-10 would not have succeeded

Lyndon Edwards  
Chair, ICRS-10

December, 2016  
Sydney, Australia.

## **Committees**

### **Local Scientific Committee:**

L. Edwards  
O. Muránsky  
C.J. Hamelin  
A. Paradowska

### **International Scientific Committee:**

Y. Akiniwa (Japan)  
K. Akita (Japan)  
S. Denis (France)  
L. Edwards (Australia)  
C. Hubbard (USA)  
Z. Kowalewski (Poland)  
J.-L. Lebrun (France)  
E. Mittemeijer (Germany)  
C. Noyan (USA)  
R. Lin Peng (Sweden)  
W. Reimers (Germany)  
P. Scardi (Italy)  
B. Scholtes (Germany)  
O. Thomas (France)  
P. Withers (United Kingdom)  
K. Xu (China)

## **Sponsors**

### **ICRS-10 Partner**

PROTO Manufacturing Ltd.  
2175 Solar Crescent Oldcastle,  
Ontario, N0R 1L0, Canada

### **ICRS-10 Sponsors**

Rigaku Corporation  
3-9-12 Matsubara-Unit 8, Akishima-Shi  
Tokyo 196-8666, Japan

VEQTER Limited  
Unicorn Business Park, Whitby Road  
Bristol, BS4 4EX, UK

Stresstech Oy  
Tikkutehtaantie  
1 40800 Vaajakoski, Finland

ANSTO  
New Illawarra Road  
Sydney NSW 2234 Australia

## Numerical Investigation of Residual Stresses in Chain-die Formed AHSS U-Channels

Yong Sun<sup>1, a</sup>, Zhen Qian<sup>1, b</sup>, Vladimir Luzin<sup>1, c</sup>, William J.T Daniel<sup>1, d</sup>,  
Mingxing Zhang<sup>1, e</sup> and Shichao Ding<sup>1, f\*</sup>

<sup>1</sup>School of mechanical and Mining Engineering, The University of Queensland, QLD, Australia

<sup>2</sup>Australian Nuclear Science and Technology Organization, Lucas Heights, NSW, Australia

<sup>a</sup>y.sun@uq.edu.au, <sup>b</sup>z.qian@uq.edu.au, <sup>c</sup>Vladimir.Luzin@ansto.gov.au, <sup>d</sup>billd@uq.edu.au,  
<sup>e</sup>mingxing.zhang@uq.edu.au, <sup>f</sup>s.ding@uq.edu.au

**Keywords:** Residual Stresses, AHSS, U-Channel, Chain-Die Forming, Finite Element Analysis

**Abstract.** Advanced high-strength steel is increasingly being used in automotive structural components due to its excellent strength-to-weight ratios. However, the variations of residual stresses magnitude in AHSS products are usually very complex and unpredictable due to the fabrication process and the material's high strength. Consequently, unbalanced residual stresses are responsible for a series of product defects. Chain-die forming is a novel AHSS fabrication method which has the characteristics of preserving the material's ductility maximally and also reducing the residual stresses in the product. In this study, the finite element method is employed to investigate the equivalent residual stresses (Von Mises) in Chain-die formed AHSS U-channels. Finite element simulation of roll forming of the same type as AHSS U-channel forming is performed to make a comparison of the residual stresses distribution characterizations in AHSS U-channels which are fabricated by roll forming and by Chain-die forming. The results indicate that the residual stresses in Chain-die formed U-channels stay at a very low level and are almost negligible. In the meanwhile, due to the bending, reverse bending and other unpredictable redundant deformation types in the roll forming process, the residual stresses are more significant than those of Chain-die formed AHSS channels. The comparison of the longitudinal strain developments of flange edges of roll formed and Chain-die formed U-channels is given to explain the differences between the residual stress distributions in the roll formed and Chain-die formed U-channels. This paper gives a comprehensive understanding of the characteristics of the residual stress distribution in Chain-die formed AHSS U-channels. It provides a clear evidence to illustrate the superiority of Chain-die forming in reducing the residual stresses in AHSS products.

### Introduction

Advanced High-Strength Steel (AHSS), especially dual phase steel, is more and more frequently being employed by automakers for structural parts of a motor vehicle due to its advantages for weight reduction and safety improvement. AHSS has the required high strength but the elongation is not large enough. The characteristics bring more challenges in fabricating AHSS products.

Roll forming is a highly efficient fabricating method for mass production of long and straight metal products. It can be understood as a continuous bending operation which the metal strips are progressively formed through consecutive sets of rolls into various profiles [1]. Although roll forming has been developed over a century, there are still unsolved issues in predictability and control of the redundant plastic deformation occurring during a roll forming process due to relaxation between roll stands [2]. Consequently, this becomes a bottleneck which greatly restricts the development and application of roll forming. Specifically, the non-uniform permanent plastic deformation results in the residual stresses in a roll formed product. The distributions of residual

stresses are responsible for a series of typical roll formed product defects and/or distortions from the desired product shapes, such as curvature, end flare, edge wave, torsion, springback and so on [3]. It should be also noted that the existence of longitudinal residual stresses would adversely affect structural stability, fatigue performance, stiffness and other properties [4].

Chain-die forming, as a novel sheet metal forming method, was therefore proposed by Ding et al. [5] to break the bottleneck of fabricating AHSS products. It is considered to have a high potential to be a more economical and energy-saving method compared to conventional roll forming, due to its technical characteristics of both bending and stamping. Ding et al. [5] performed a series of experiments of Chain-die forming AHSS U-channels with pre-made holes. They proved that the technology has the advantage of conserving the material's ductility. This shows that Chain-die forming can be used to fabricate AHSS products, even though some of them have poor ductility, as there is almost no redundant plastic deformation and low residual stresses in the non-deformed areas.

As Ding et al. [5] introduced, the principle of Chain-die forming is to prolong the effective forming distance by extending the virtual roll radii. Specifically, the technology introduces a series of discontinuous forming tools moving on a track board to implement the virtual large rolls, as seen in Fig. 1 (a). The increase of deformation length shown as in Fig. 1 (b) results in the reduction of the peak longitudinal strain and the residual longitudinal strain. That is, the large roll radii can significantly reduce or even eliminate the redundant plastic deformation occurring in roll forming. Consequently, the corresponding residual stresses are significant reduced. The typical defects of roll formed products can be therefore theoretically removed, thus improving the quality of products.

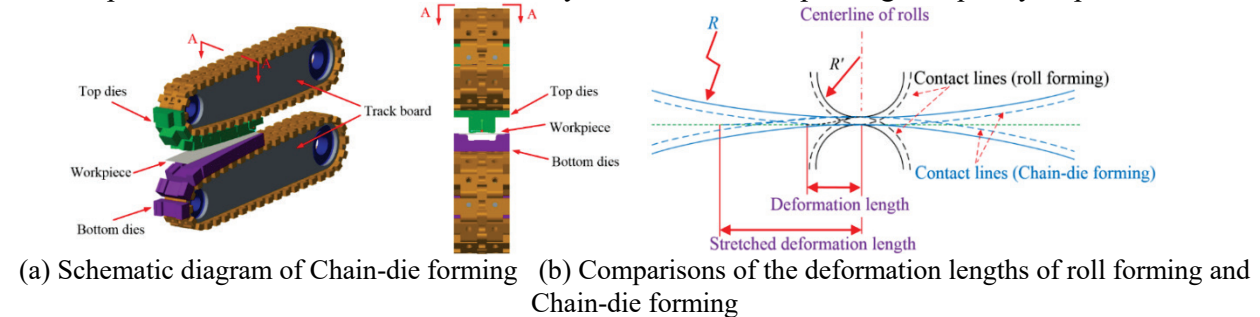


Fig 1. The principle of Chain-die forming. (Note:  $R$  are the radii of the top and bottom rolls of Chain-die forming and  $R'$  is the radius of a roll of conventional roll forming)

The structure of the paper is as follows. A brief background of residual stresses in roll forming and the principles of Chain-die forming are introduced in this section firstly, followed by the clarifications of finite element (FE) modeling of roll forming and Chain-die forming AHSS U-channels. Then the equivalent residual stresses (Von-Mises) in the non-deformation areas of roll formed and Chain-die formed AHSS U-channels are investigated. The comparison of the longitudinal strain developments of the flange edges of roll formed and Chain-die formed AHSS U-channels are then studied and discussed. Finally, some important concluding remarks are summarized.

### FE modeling

The FE modelling of roll forming and Chain-die forming the U-channels with same product parameters are introduced in detail in this section. Then the material properties of the working piece adopted in this study are illustrated followed by the clarifications of the contact properties employed between the forming tools and the workpiece.

### Simulation set-up.

The simulation verifications were carried out in ABAQUS/Standard. Specific python scripts were imported to ABAQUS/CAE to complete the FE modelling processes. The implicit solution algorithm is employed to improve the accuracy of results. The forming tools are defined as the rigid shell

bodies and the workpiece is defined as a deformable body. Taking advantages of symmetry to improve the computing efficiency, only one half of the workpiece and rolls have been modelled.

In FE modelling of the roll forming process, all the base radii of the forming tools are 0.30m. The center points of the rolls were assigned as the reference rotation points of the corresponding forming tools respectively. The angular velocities,  $\omega$ , of the rotations of the forming tools were set as the 0.5rad/s, and in meanwhile the horizontal forward velocity of the working piece,  $v$ , was set as 15mm/s ( $v = \omega r$ ). As the main plastic deformation occurs in the bend corners, the initial flat blank had been meshed using different mesh sizes. A very fine mesh has been adopted in the bend corners and flange edge portions and a coarse mesh had been applied in the web of the blank. The workpiece was meshed with 97500 eight node linear brick elements with reduced integration and hourglass control (C3D8R). There were 5 mesh layers (elements) along the thickness direction to guarantee a good convergence. To avoid penetration into the sheet, the mesh type of the forming tools was the four node 3D bilinear rigid quadrilateral element (R3D4).

In FE modelling of Chain-die forming process, the forming tools were part of the rolls with 35 meter radii. A workpiece identical to the one applied in FE modelling of roll forming process was adopted in FE modelling of Chain-die forming process. The same meshing strategies and similar boundaries conditions were applied in the FE model of Chain-die forming process. The details of the FE models of roll forming and Chain-die forming processes and the mesh of the workpiece are shown in Fig.2 (a) and (b) respectively.

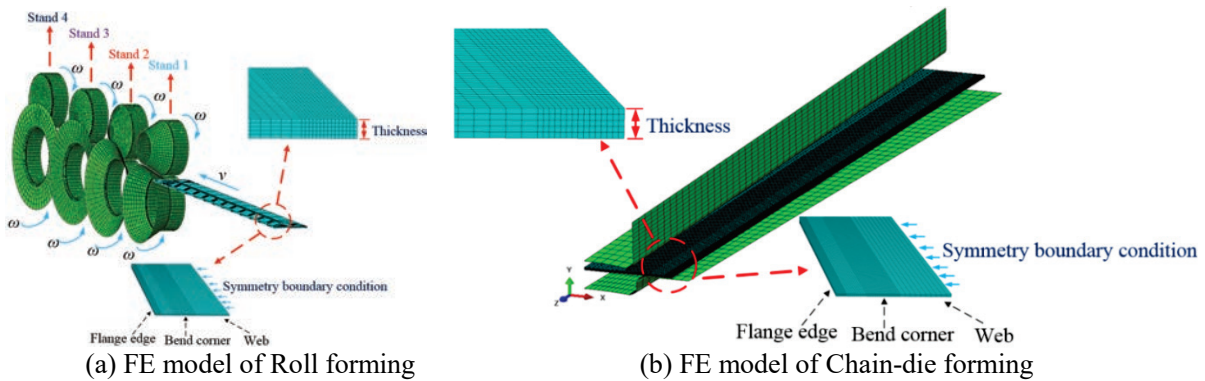


Fig 2. FE models of roll forming and Chain-die forming

### Material properties of the workpiece.

Material used in the FE models is an elastic-plastic strain hardening material. The true plastic stress-strain curve of the sheet metal can be calculated and interpolated using Swift's isotropic strain hardening law, as shown in Eq.1. As isotropic hardening is applied in all simulations, Von Mises yield function is sufficient to describe the yield criteria of the material.

$$\sigma_e = K (\varepsilon_e + \varepsilon_0)^n \quad (\text{Eq.1})$$

where  $\sigma_e$  is the equivalent stress,  $\varepsilon_e$  is the equivalent strain,  $\varepsilon_0$  is the initial strain,  $K$  is the strength coefficient and  $n$  is the strain hardening exponent. Those values are given in Table 3.

### Contact and friction properties between forming tools and workpiece.

The types of interaction are set as 'surface-to-surface' (implicit) contacts between the deformable surfaces (sheet metal) and the rigid surfaces (forming tools). The penalty method and the Coulomb friction model are applied to the contact constraints. The friction coefficient of the FE models is assumed as 0.1. The details of the parameters of the FE models have been summarized in Table 1.

Table 1. Summary FEM simulation parameters

Simulation Parameters	Chain-die forming	Roll forming
Product width - $f$ (mm)	80	80
Roll radius (mm)	35000	30
Blank thickness - $t$ (mm)	1.2	1.2
Blank length - $L$ (mm)	300	300
Tensile strength of blank - $TS$ (MPa)	1180MPa	1180MPa
Algorithm method	Implicit	Implicit
Mesh number (blank)	13050	13050
Span space (mm)	---	200
Yield strength - $\sigma_s$ (MPa)	845	845
Strength coefficient - $K$ (MPa)	1864	1864
Young's modulus - $E$ (GPa)	206	206
Poisson's ratio - $\nu$	0.3	0.3
Initial strain - $\epsilon_0$	0.000367	0.000367
Strain hardening exponent - $n$	0.11	0.11
Elastic Strain	0.45%	0.45%

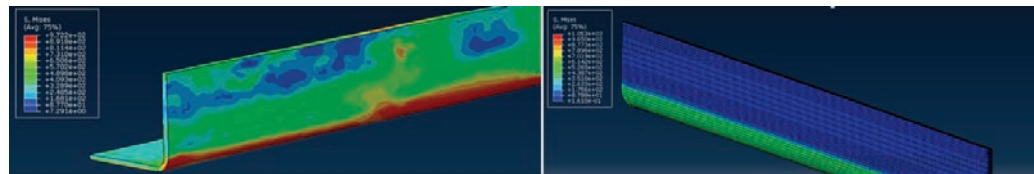
In the FE model of roll forming and Chain-die forming processes, the whole simulations include the loading and unloading processes. Specifically, the workpiece was firstly pulled into the former followed by being gradually formed to a U channel by the friction forces with the rotations of the forming tools, the same as the real forming process. The accumulated stress-strain of the workpiece starts to be released by springback while the forming tools move away from the workpiece. The workpiece with the last stress-strain state in the previous model is finally imported into a new simulation model with an implicit solution algorithm. The stress-strain of the workpiece is further released by springback until it reaches a steady state in the new FE model.

**Results and discussions**

The equivalent residual stresses (Von-Mises) in AHSS U channels induced by roll forming and Chain-die forming are presented and discussed in details in this section. The comparison of the longitudinal strain developments of flange edges of roll formed and Chain-die formed U channels is also clarified to explain the phenomenon.

**Equivalent residual stresses comparison.**

The residual stresses in AHSS U-channels induced by roll forming and Chain-die forming are presented in Fig.3 (a) and Fig.3 (b) respectively. As shown in Fig.3 (b), the residual stresses in non-deformation areas of Chain-die formed U-channels are negligible while there are significant and uneven residual stresses distribution in non-deformation areas of roll formed AHSS channels.



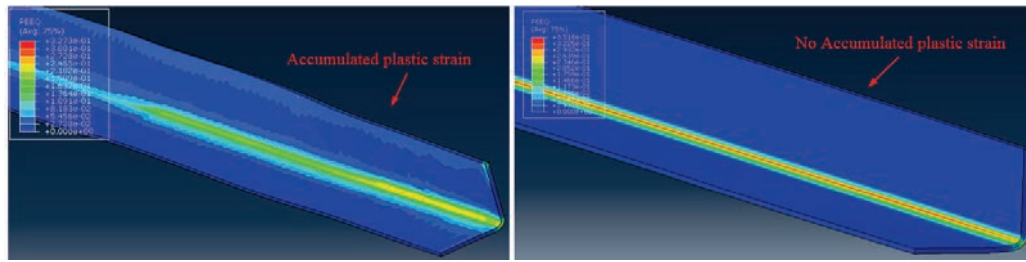
(a) Roll formed U-channels

(b) Chain-die formed U-channels

Fig 3. Equivalent residual stresses comparison

As the Chain-die forming process can be considered as a gradually stamping process, there are nearly no redundant deformations in Chain-die forming process. Consequently, the low residual

stresses in Chain-die formed U-channels are accumulated and the product defects induced in roll forming process can therefore be avoided, as seen in Fig.4.



(a) Roll formed U channels

(b) Chain-die formed U channels

Fig 4. Equivalent residual plastic strain comparison (PEEQ)

### Longitudinal residual strains comparison.

As the longitudinal strain development indicates the severity of the relevant forming process, it can be used to explain the characteristic differences of the residual stress distributions in two types of AHSS U-channels. The comparison of the longitudinal strain developments of flange edges of Chain-die formed and roll formed the AHSS U-channels is shown in Fig.5. It is found that the longitudinal strain developed during Chain-die forming is much smoother, the peak strain and residual strain are smaller than in roll forming, even just in one forming pass rather than 4 passes of roll forming. The unavoidable redundant plastic deformation in a roll forming process can also be avoided in Chain-die forming.

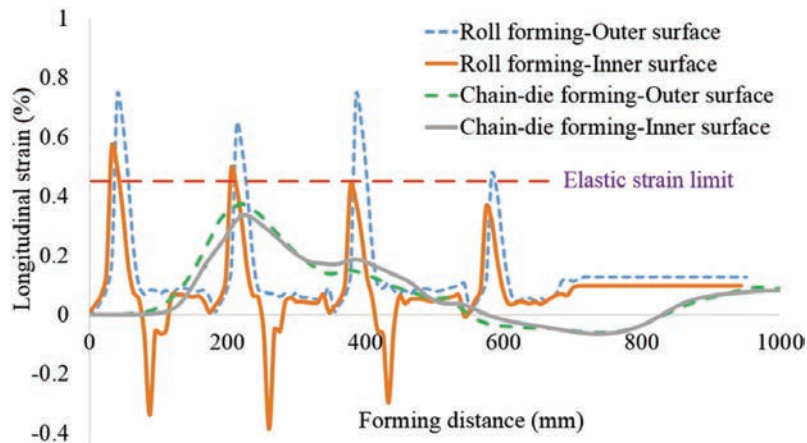


Fig 5. The longitudinal strain development between roll formed and Chain-die formed U-channels

As shown as in Fig.5, the peak longitudinal strain in the roll forming process is nearly 2 times larger than that in the Chain-die forming process. It should be noted that the bending on the flange phenomenon in Chain-die forming is much lighter and gentler than in roll forming, the corresponding bending strain is much smaller than in roll forming. That is, the surface longitudinal strain superposing the membrane strain and bending strain on the flange during Chain-die forming is well below the material's elastic limit but not in roll forming. It is therefore hard to predict and control the quality of a roll formed product due to its complicated longitudinal strain development. On the contrary, it is possible to make a product with zero residual stress in the non-deformed area by Chain-die forming and give a better quality product than in roll forming.

## Concluding Remarks

The residual stresses in Chain-die formed AHSS U-channels are investigated numerically in this paper. Finite element analysis is employed to simulate the roll forming and Chain-die forming processes. The equivalent residual stresses of the roll formed and Chain-die formed products are discussed. Experimental investigation of the residual stresses in Chain-die formed U-channels is very necessary to verify the simulations. Some conclusions are reached by this study:

- Using Chain-die forming can achieve much more bending without product defects than roll forming in a single pass. Hence Chain-die forming can maximally reserve the material's ductility;
- Unlike the high residual stresses distribution in the non-deformation areas in roll formed U-channels, the low redundant strains accumulated in Chain-die formed forming makes the residual stresses in U-channels well below the corresponding material's yield point;
- It is hard to predict the residual stresses in roll formed product due to its complicated fabrication processes, including bending, reverse bending and other unnecessary deformation types. On the contrary, it is possible to make a product with zero residual stress in the non-deformed area by Chain-die forming and that gives a better quality product than in roll forming.

The determination of residual stresses in Chain-die formed U-channels by the neutron diffraction method is currently in progress and the experiments are supported by Bragg Institute beam time proposal 4865. The experimental verification of the numerical simulations will be presented in a future paper.

## Acknowledgement

The authors would like to thank for the financial support from the Baosteel-Australia Joint Research and Development Centre (BAJC), Ningbo SaiRolf Metal Forming Co., Ltd., Bragg Institute beam time proposal 4865 and China Scholarship Council. Colleagues who contributed their efforts and support to this paper are also appreciated. Finally, the authors would like to give special thanks to Baosteel Co.,Ltd. for providing the material properties of the experimental samples.

## References

- [1] Paralikas, J., Salonitis, K., Chryssolouris, G., 2009. Investigation of the effects of main roll-forming process parameters on quality for a V-section profile from AHSS. *The International Journal of Advanced Manufacturing Technology* 2009, 44(3-4), 223-237.  
<http://dx.doi.org/10.1007/s00170-008-1822-9>
- [2] Panton, S. M.; Zhu, S. D.; Duncan, J. L. Fundamental deformation types and sectional properties in roll forming. *International journal of mechanical sciences* 1994, 36(8), 725-735.  
[http://dx.doi.org/10.1016/0020-7403\(94\)90088-4](http://dx.doi.org/10.1016/0020-7403(94)90088-4)
- [3] Semiatin, S.L. *ASM Handbook*; American Society for Metals: Materials Park, United States, 1988; 2110 pp.
- [4] Hou, G., Jing, X., Yan, D., & Shen, K. Prediction of longitudinal residual stress distribution in cold-formed square hollow sections. In *Electric Technology and Civil Engineering (ICETCE)*, 2011 International Conference on (pp. 557-562). IEEE.
- [5] Zhang, Y. Ding, S., 2012. A comparison study of Chain-die Forming and roll forming by forming a top hat section. *Proceedings of the 14th International Conference on Metal Forming*, Wiley, London, England, 703-706.

# Quasi-static Process Modelling of Deep Cold Rolling on Ti-6Al-4V

A. Lim<sup>1,2,a\*</sup>, S. Castagne<sup>1</sup>, C.C. Wong<sup>2</sup>

<sup>1</sup>School of Mechanical and Aerospace Engineering, Nanyang Technological University, Singapore

<sup>2</sup>Advanced Technology Centre, Rolls-Royce Singapore Pte Ltd, Singapore

<sup>a</sup>lims0200@e.ntu.edu.sg

**Keywords:** Deep Cold Rolling, Residual Stress Modelling Methods, Residual Stresses in Manufacturing Process, Simulation, Abaqus

**Abstract.** This paper proposes a 3D Finite Element (FE) model for the deep cold rolling process, modelled using the commercially available Abaqus/Standard FE software, and used the aforementioned model to study the effects of pressure and tool diameter on the residual stress profile predicted. The model was validated with experimental data. The predicted results showed about 20% deviation for the measured data in the near surface region, but showed good correlation at the compressive-tensile cross-over point. Reasons for this deviation are explored and analysed with several recommendations made to improve future FE models.

## Introduction

Mechanical surface treatment (MST) methods physically alter the surface and near sub-surface regions of a component, creating a region of compressive residual stress. This compressive residual stress improves fatigue life and foreign object damage tolerance. Deep cold rolling (DCR) is a mechanical surface treatment and its main objective is to induce deep compressive residual stresses in the surface and sub-surface layers (up to 1 mm) of the component [1].

While the high compressive stresses generated by DCR in the near surface layers can extend fatigue life, it is crucial that the location and magnitude of the corresponding balancing tensile residual stresses are carefully managed and understood, as they can negate the benefits of the near surface compressive residual stress and adversely affect the fatigue life of the component [2]. However, experimental determination of residual stress distributions by the hole drilling method and the X-ray diffraction method is time consuming, expensive and limited to discrete measurement points. Hence, FE simulation is a crucial tool in the process optimization of the DCR method as it allows the user to analyse and predict the residual stress profile of the component.

DCR creates different directional stress profiles and is reliant on both plastic deformation at the surface and Hertzian stress at the sub-surface region to generate the resultant residual stress profiles. Previous quasi-static finite element studies of the DCR process focused on the mechanics of a single pass [3]. While useful for understanding the mechanics of the DCR process, modelling of a single pass is insufficient to study the broader residual stress distributions.

The objective of this study is to propose and validate a FE model to simulate the DCR process. This model will enable a deeper understanding of the broader residual stress distributions caused by the DCR process.

## Methodology

**Material Model.** The material model attributed to the model is isotropic elastic-plastic with strain hardening. A Young's modulus of 113.8 GPa and a Poisson ratio of 0.342 are prescribed for the elastic portion of the material model. The strain hardening portion of the material model was

experimentally determined via uniaxial compression of identical Ti-6Al-4V material in cylinder geometry measuring 6.75 mm height by 4.5 mm diameter. The machine stiffness is taken into account using plate to plate compression. Figure 1 shows the determined yield stress against plastic strain.

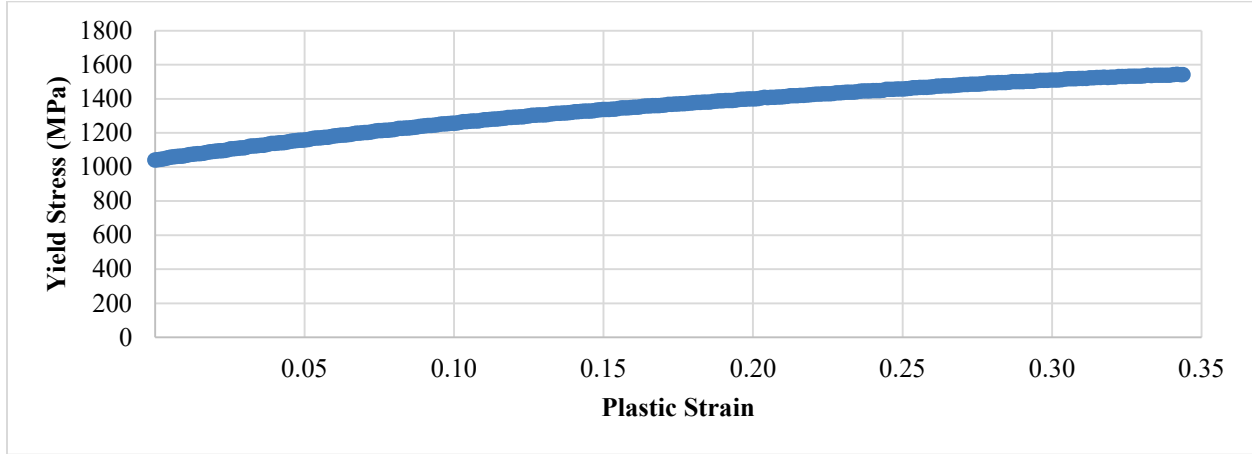


Figure 1: Yield stress against plastic strain for Ti-6Al-4V

Finite Element Model. The FE DCR model proposed is a 3-dimensional rectangular test coupon measuring 35 mm x 30 mm x 10 mm. commercially available FE code Abaqus/Standard V6.14 was used to model the test coupon. The 3D deformable element type used was the C3D8R element, an 8-node linear brick, using 56916 elements to model the test coupon. Uniform elements were used in the DCR zone to increase the resolution of the treated area, as shown in Figure 2a. Sensitivity analysis on the thickness of the test coupon was carried out to ensure that the thickness did not affect the residual stress profile generated.

To reduce computational time, a treated area of 15 mm lengthwise (LW – parallel to direction of rolling) by 10 mm crosswise (CW – perpendicular to direction of rolling) was prescribed. The deep cold rolled zone allowed enough area for a strain gage rosette to be applied onto the experimental test block for experimental validation.

The DCR tool is made of tungsten carbide and has a Vickers hardness of approximately 2000 HV. Since this is several orders of magnitude harder than the test coupon, the tool was modelled as an analytical rigid surface. The centre node of the modelled tool was used as the main reference and control point. The equivalent concentrated force can be calculated using the following formula:

$$F = \left[ \frac{\pi}{4} * d_{piston}^2 * P \cos(\theta) \right] \tag{1}$$

where,  $d_{piston}$  is the piston diameter, P is the applied pressure and  $\theta$  is the angle of the tool to the normal.

The movement of the ball is controlled via translating the centre node of the ball, in the length and breadth direction. The DCR tool has an inner assembly containing the burnishing ball which is free floating (as shown in Figure 2b). The force prescribed determines the vertical position of the ball, relative to the component surface at equilibrium. Therefore, the displacement of the ball in the Z direction (normal to surface of the component) was left free. This is to mimic the operating mechanics of the DCR tool where the inner tool assembly is free to move in an up and down motion within the outer tool housing up to the limits of the stroke length. This allows the DCR tool to adapt to minor variations in geometry.

The rotational degrees of freedom of the ball were also left free, ensuring that the ball is able to roll across the surface. The penalty formulation with a friction coefficient of 0.2 was used to model the surface to surface contact between the DCR ball and the work piece [4]. This also ensures that the ball rolls rather than slides across the component surface.

The boundary conditions were imposed such that the bottom surface of the test coupon is pinned. Since the test coupon is of sufficient thickness, it was assumed that the spring back of the coupon after treatment is negligible. The dimensions of the test coupon, the mesh, elements used and the boundary conditions are illustrated in Figure 2.

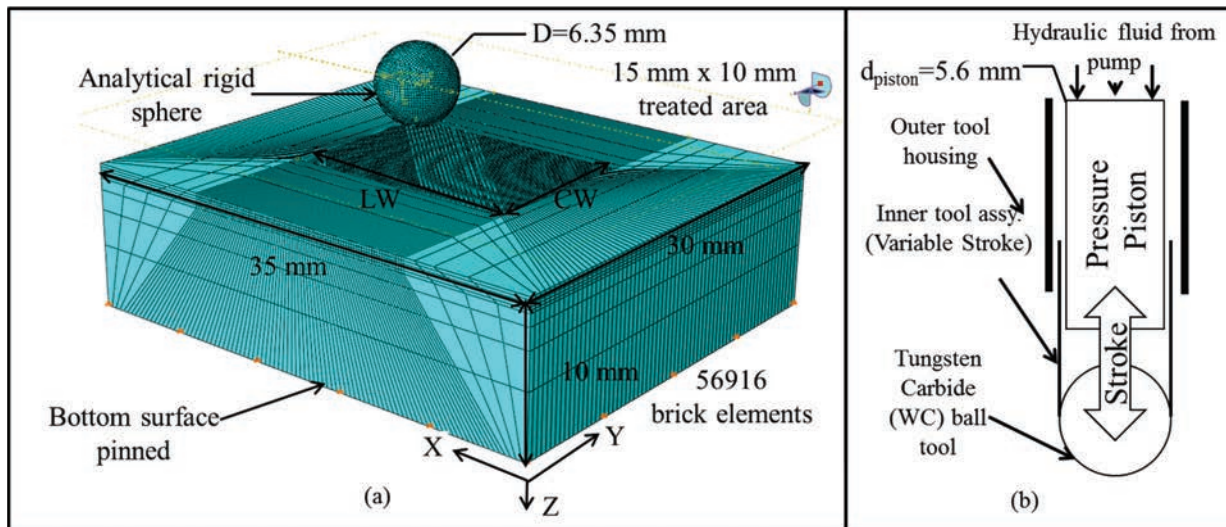


Figure 2: (a) Finite element model and set-up and (b) schematic of DCR tool

Experimental Setup and DCR Tool. Experiments were carried out to validate the proposed FE model. A flat rectangular test coupon of Ti-6Al-4V, measuring 35 mm x 30 mm x 20 mm was mounted on a work piece holding fixture and deep cold rolled. The DCR tool (6.35 mm ball diameter), supplied by Ecoroll AG®, at 20.0 MPa and 38.0 MPa of pressure was used to perform the treatment. The test coupon was orientated such that the rolling direction of the DCR process is identical to the rolling direction that was used in the manufacturing of the test coupons. Figure 3 shows the DCR process experimental set up.

The residual stress profile of the test coupon was determined at the centre of the treated area using the central hole drilling method (CHD). The strain relaxation via the incremental drill method was measured and the residual stresses were back calculated as described in ASTM 837. A final hole depth of 1.4mm was drilled in order to determine the stresses up to a depth of 1024µm.

## Results and Discussion

FE Model Validation. The finite element model was validated using experimental CHD data. In this study, the experimental and finite element data was normalized against the absolute maximum residual stress determined experimentally in the CW direction. The normalized graph is presented in Figure 4.

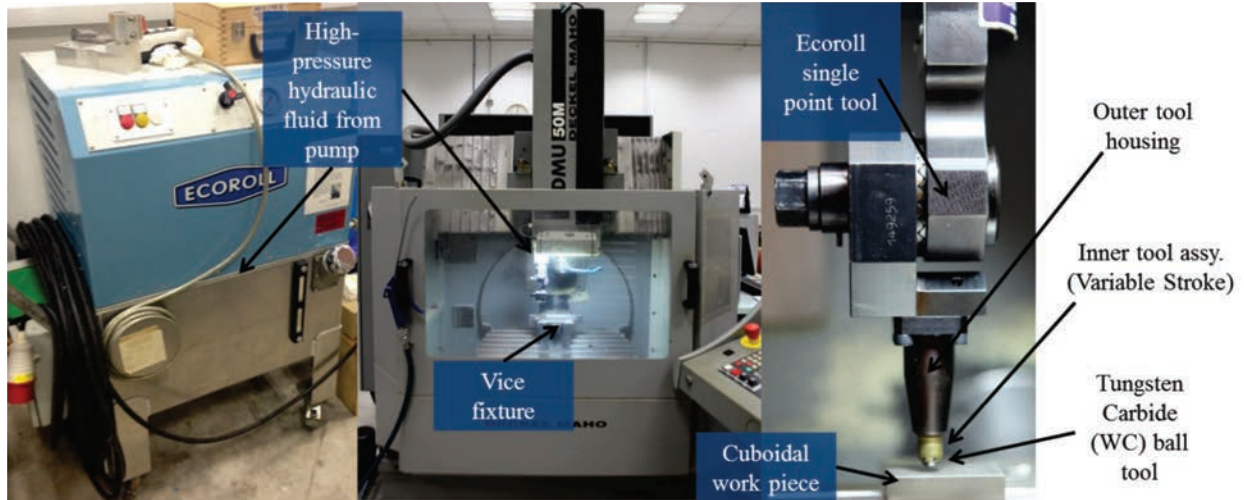


Figure 3: Experimental DCR set-up on a 3-axis CNC mill

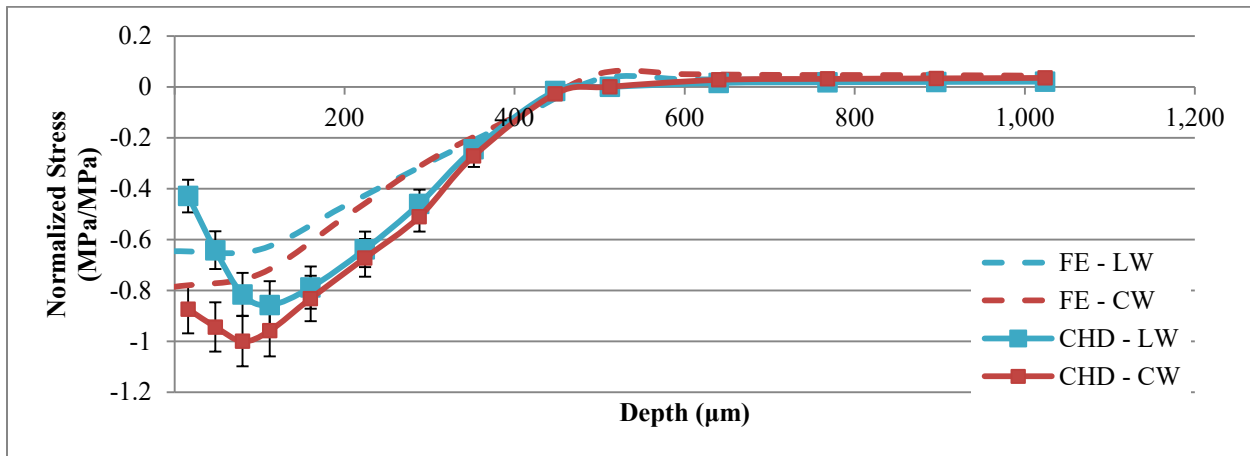


Figure 4: Normalized residual stress against depth for experimental and simulation data for 20.0 MPa

From Figure 4, it can be seen that there is some divergence of the residual stress in the near surface region. The FE model over-predicted the surface stress in the LW direction (parallel to rolling) at -0.43 MPa/MPa measured against -0.63 MPa/MPa predicted, and under predicted the surface stress in the CW direction (perpendicular to rolling) at -0.87 MPa/MPa measured against -0.78 MPa/MPa predicted. Figure 5 shows the residual stress profiles when the pressure is increased to 38.0 MPa. There is a similar deviation between the measured and predicted residual stress profiles for both cases.

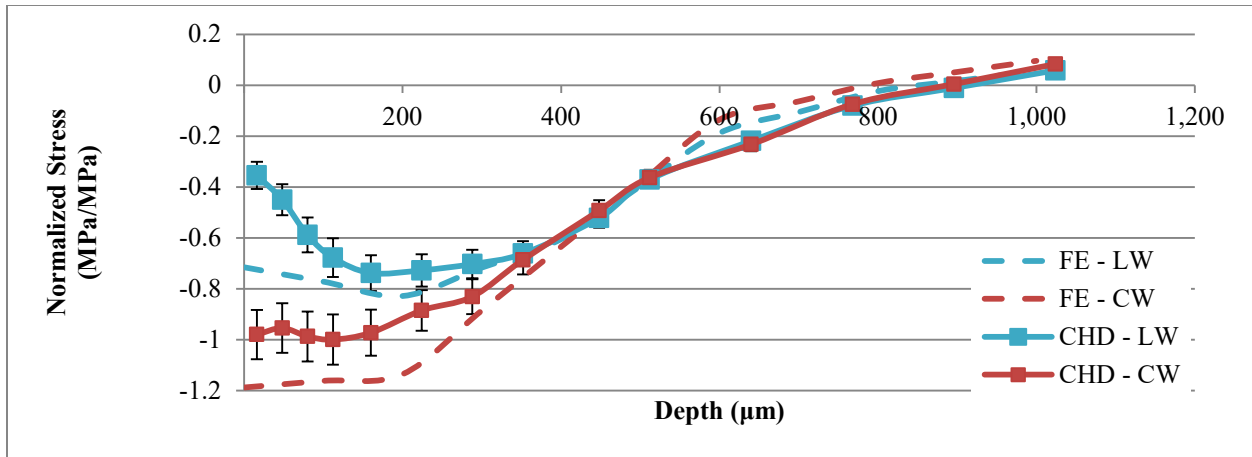


Figure 5: Normalized residual stress against depth for experimental and simulation data for 38.0 MPa

Deeper into the material, both FE models are able to predict the general trend of the residual stress profile and the Compressive-Tensile Cross-Over point (CTCO). The CTCO point is of particular importance as the location of the balancing tensile stress needs to be able to be understood and predicted.

Regarding the deviation between the FE and CHD data, the material model used assumed that the material was isotropic. Further compression tests taking into account the rolling direction of the manufacturing process should be carried out to determine if this simplifying assumption holds valid. A more detailed model, such as the Johnson-Cook model, could be considered for future FE simulations.

In this study, the implicit FE code is used and it does not take time into consideration when performing iterations. The time step used in the code relates to the relative position of the components and forces applied rather than actual time as a parameter. The implicit code does not take strain rate into consideration

Another potential cause of the deviation could be the measurement method used to determine the experimental residual stress profiles. While CHD is an affordable and quick way of determining residual stress depth profiles, it has limited resolution in the near surface region (up to about 200 μm). This can be seen in the error bars shown in Figure 4 for the experimental graphs. At the near surface region, CHD has an error of about 10 – 15%  $\sigma_{max}$ . X-ray diffraction (XRD) or Focused Ion Beam (FIB) methods could potentially be used to attain more accurate data in the near surface region.

A final source of error that may have resulted in the deviation is the concentrated force applied based on equation (1). The equation calculates the theoretical force exerted by the DCR ball element on the component based on the pressure applied and the projected area of the pressure piston. A dynamometer could be placed under the component fixture to determine the actual force applied on the test coupon. This measured force can then be used to further improve the FE model.

The motivation behind process modelling the DCR process can be seen in the stress plots of the component shown in Figure 6. There is a zone of tensile residual stress that was formed near the boundary region at 1.0mm in depth for the 38.0 MPa case that was not present for the 20.0 MPa case. Knowledge of this zone of tensile stress will assist the process engineer in designing of the DCR zone and ensure that the component does not prematurely fail due to the tensile stress.

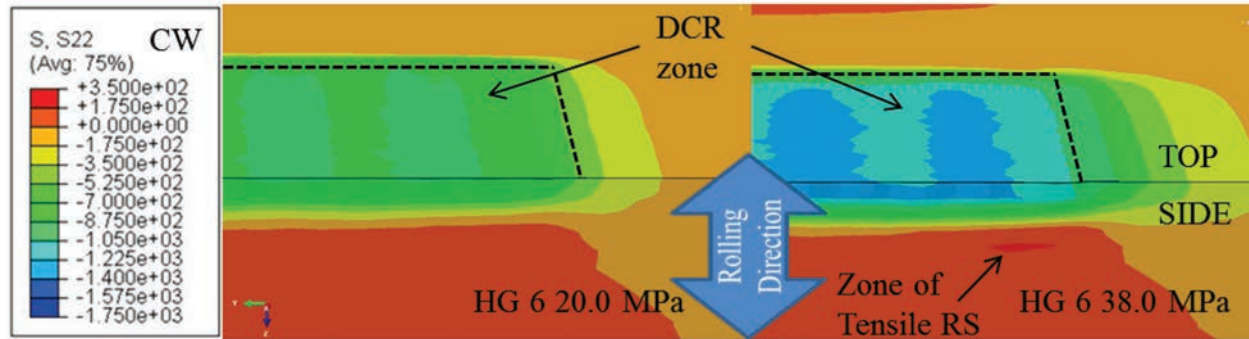


Figure 6: FE stress plot for HG 6, 20.0 MPa and 38.0 MPa, cut at  $x = 17.5$  cm (centre of treated zone)

### Conclusion

This paper proposed a 3D FE model to simulate the DCR process. There is a maximum deviation of 0.2 MPa/MPa at the surface region between the predicted FE results and the CHD measured data. There is good agreement between the FE and CHD data beyond 400  $\mu\text{m}$ . Some causes of the deviation between the FE predicted values and the experimental data have been proposed and will need to be verified. Different material models will be studied in order to better understand the effects of the material models on the accuracy of the FE simulation.

### Acknowledgement

This study was conducted using funding from the Singapore Economic Development Board (EDB) and Rolls-Royce Singapore Pte. Ltd. Joint Industrial Post-graduate Programme (IPP) grant. Finite element modelling for this study was conducted in Computer Aided Engineering Laboratory 1 of School of Mechanical and Aerospace Engineering, Nanyang Technological University.

### References

- [1] Altenberger, I. Deep rolling—the past, the present and the future. in Proceedings of 9th International Conference on Shot Peening, Sept. 2005.
- [2] Webster, G. and A. Ezeilo, Residual stress distributions and their influence on fatigue lifetimes. *International Journal of Fatigue*, 2001. **23**: p. 375-383.  
[http://dx.doi.org/10.1016/S0142-1123\(01\)00133-5](http://dx.doi.org/10.1016/S0142-1123(01)00133-5)
- [3] Balland, P., et al., Mechanics of the burnishing process. *Precision Engineering*, 2013. **37**(1): p. 129-134.  
<http://dx.doi.org/10.1016/j.precisioneng.2012.07.008>
- [4] Lim, A., S. Castagne, and C.C. Wong, Effect of Friction Coefficient on Finite Element Modeling of the Deep Cold Rolling Process, in Shot Peening: 12<sup>th</sup> International Conference, ICSP 12, Goslar, Germany, September 2014, Proceedings, L. Wagner, Editor. 2014: Clausthal-Zellerfeld, Germany. p. 376-380.

# Effect of Cooling and Shot Peening on Residual Stresses and Fatigue Performance of Milled Inconel 718

Zhe Chen<sup>1, a \*</sup>, Ru Lin Peng<sup>1, b</sup>, Johan Moverare<sup>1, c</sup>, Olle Widman<sup>2, d</sup>,  
David Gustafsson<sup>3, e</sup>, Sten Johansson<sup>1, f</sup>

<sup>1</sup>Division of Engineering Materials, Linköping University, 58183 Linköping, Sweden

<sup>2</sup>Ytstruktur Arboga AB, 73222 Arboga, Sweden

<sup>3</sup>Siemens Industrial Turbomachinery AB, 61283 Finspång, Sweden

<sup>a</sup>zhe.chen@liu.se, <sup>b</sup>ru.peng@liu.se, <sup>c</sup>johan.moverare@liu.se, <sup>d</sup>olle.widman@ytstrukturarboga.se,  
<sup>e</sup>david.gustafsson@siemens.com, <sup>f</sup>sten.johansson@liu.se

**Keywords:** Residual Stresses, Surface Integrity, Milling, Shot Peening, Superalloys, Fatigue

**Abstract.** The present study highlights the effect of cooling and post-machining surface treatment of shot peening on the residual stresses and corresponding fatigue life of milled superalloy Inconel 718. It was found that tensile residual stresses were created on the milled surface, regardless of the use of coolant, however, the wet milling operation led to a lower surface tension and a reduced thickness of the tensile layer. The shot peening performed on the dry-milled specimens completely annihilated the surface tensile residual stresses and introduced a high level of surface compression. A comparable fatigue life for the wet-milled specimens was obtained as compared with the specimens prepared by dry milling. This is very likely attributed to that the milling-induced surface damage with respect to cracked non-metallic inclusions is the predominant cause of the fatigue failure. The presence of the compressive layer induced by shot peening resulted in a significant increase of the fatigue life and strength, while the extent to which the lifetime was prolonged was decreased as the applied load was increased.

## Introduction

Fatigue is one of the main causes of failure to various structures in turbine engines. The fatigue life of a component strongly depends on its surface condition produced by machining since in most cases fatigue crack initiation starts on free surfaces. Residual stress is one of the most relevant practical parameters to assess the surface quality of a machined surface; it is superimposed on the applied cyclic loads, altering the driving force for crack initiation and propagation during fatigue. Generally, tensile residual stresses are perceived to be detrimental to the fatigue performance, whereas compressive residual stresses have a beneficial effect. The formation of residual stresses in machining processes is essentially dominated by the plastic deformation in subsurface of the workpiece material together with the thermal impact at surface [1]. The thermally-induced residual stresses are usually in tension, thus sufficient cooling could effectively reduce the surface tension on a machined surface by lowering the cutting temperature, or even introduce compressive residual stresses [2].

On the other hand, mechanical surface treatments, such as shot peening, are nowadays widely used on machined components by which compressive residual stresses are induced as it produces a work-hardened layer and misfit strains between the bulk and surface material. An enhanced fatigue life and strength by shot peening have been found for a variety of engineering materials [3-5].

Inconel 718 is a polycrystalline nickel-based superalloy and has wide applications in aerospace and power generation industries because of its superior mechanical properties and good resistance to oxidation/corrosion environments. A great number of studies have been conducted to improve the surface integrity of machined Inconel 718 by approaches with process optimization or post-machining surface treatments (like shot peening) [6]. However, further investigations on the effect of changes in

surface integrity on the fatigue properties of the components are somewhat limited although it has a great practical importance for the assessment of the component life and also the knowledge obtained can be used backwards to guide the surface integrity modification. The purpose of the current study is to characterize the residual stresses generated on milled Inconel 718 as influenced by the use of coolant and a subsequent shot-peening treatment. Meanwhile, the fatigue performance of the specimens corresponding to the different surface conditions has also been studied in a four-point bending mode.

### Experimental work

The material used in this study was taken from a disc forging of Inconel 718 with chemical composition given in Table 1. The forging was solution annealed at 970 °C followed by air cooling to room temperature, and then a two-stage ageing was performed first at 720 °C for 8 h, further at 620 °C for another 8 h, and finally air cooled to room temperature.

*Table 1. Chemical composition [wt%] of the Inconel 718 disc forging.*

	Fe	Ni	Cr	Mo	Nb	Ti	Al	C
Min. (%)	Bal.	50	17	2.8	4.75	0.65	0.2	
Max. (%)		55	21	3.3	5.5	1.15	0.8	0.08

Fatigue test bars with a dimension of  $10 \times 10 \times 80 \text{ mm}^3$  were pre-manufactured from the heat-treated forging by wire electric discharge machining. The surface to be loaded in tension during fatigue was then machined by face milling using a 20 mm diameter cutter with two uncoated cemented carbide inserts. The cutting speed was fixed at 30 m/min (corresponding spindle speed was 382 rpm) and the depth of cut was 0.5 mm. The feed direction was along the longitudinal direction of the bar with a feed rate of 76 mm/min. Chamfers on the tensile side were introduced in order to avoid corner crack initiation. Three groups of specimens were prepared; the specimens of the first two groups were dry milled and milled under coolant respectively, while for the last group, the surface that has been machined by dry milling was subsequently shot peened using spherical S170 H cast steel shots with 150 to 200 % surface coverage, while the shot-peening intensity was varied from 0.2 to 0.3 mmA.

The microstructure beneath the dry-milled, wet-milled and shot-peened surface was characterized on polished cross-sections prior to fatigue testing using a scanning electron microscope (SEM) together with electron channeling contrast imaging (ECCI). In addition, the In-depth residual stresses created by milling and shot peening were measured by using X-ray diffraction, combined with layer removal by electrolytical polishing. Cr-K $\alpha$  radiation was chosen, giving a diffraction peak at  $2\theta \sim 128^\circ$  for the {220} family of lattice planes of the nickel-based matrix. Peaks were measured at nine  $\psi$ -angles between  $\psi = \pm 55^\circ$ , and residual stresses were calculated based on the “ $\sin^2 \psi$ ” method [7] with an X-ray elastic constant of  $4.65 \times 10^{-6} \text{ MPa}^{-1}$ . Deviation in the measured residual stresses due to the layer removal were corrected in the case of a flat plate.

All fatigue tests were conducted at room temperature under load control using a sinusoidal waveform at a load ratio of 0.1 and a frequency of 20 Hz. The distance between the two loading and two supporting rollers was 12 mm and 60 mm, respectively. For each group of the three, four specimens were tested at different peak loads in the range of 8 kN to 16 kN. The corresponding peak stress at the surface, calculated assuming pure elastic loading, were approximately 600 MPa to 1200 MPa. The yield strength of the Inconel 718 forging at room temperature, on the other hand, is slightly above 1000 MPa. All specimens were fatigued until rupture and the specimen deflection at the maximum/minimum load versus the number of cycles was recorded. A line was fitted to the initial linear part of the deflection range-number of cycles curve and extrapolated to the larger cycle region. The number of cycles corresponding to 1% increase of the deflection range from the fitted line was then defined as the fatigue life in the present study. Accordingly, the lifetime of the specimens is largely dominated by the fatigue cycles spent on crack initiation. The failed specimens were examined under SEM in order to identify the preferential sites where fatigue cracks may initiate.

### Results and discussions

Fig. 1(a) and (b) shows the in-depth residual stresses induced by dry milling and wet milling. Stress components in two in-plane directions, i.e. transverse direction (TD) and longitudinal direction (LD) (corresponding to the cutting direction and feed direction), were measured. In general, tensile residual stresses were created on the milled surface, regardless of the application of coolant, but it is clear that the wet milling operation led to a lower surface tension and a reduced thickness of the tensile layer. As the depth increases, the residual stresses gradually shift to compression until stabilizing at ~ 0 MPa.

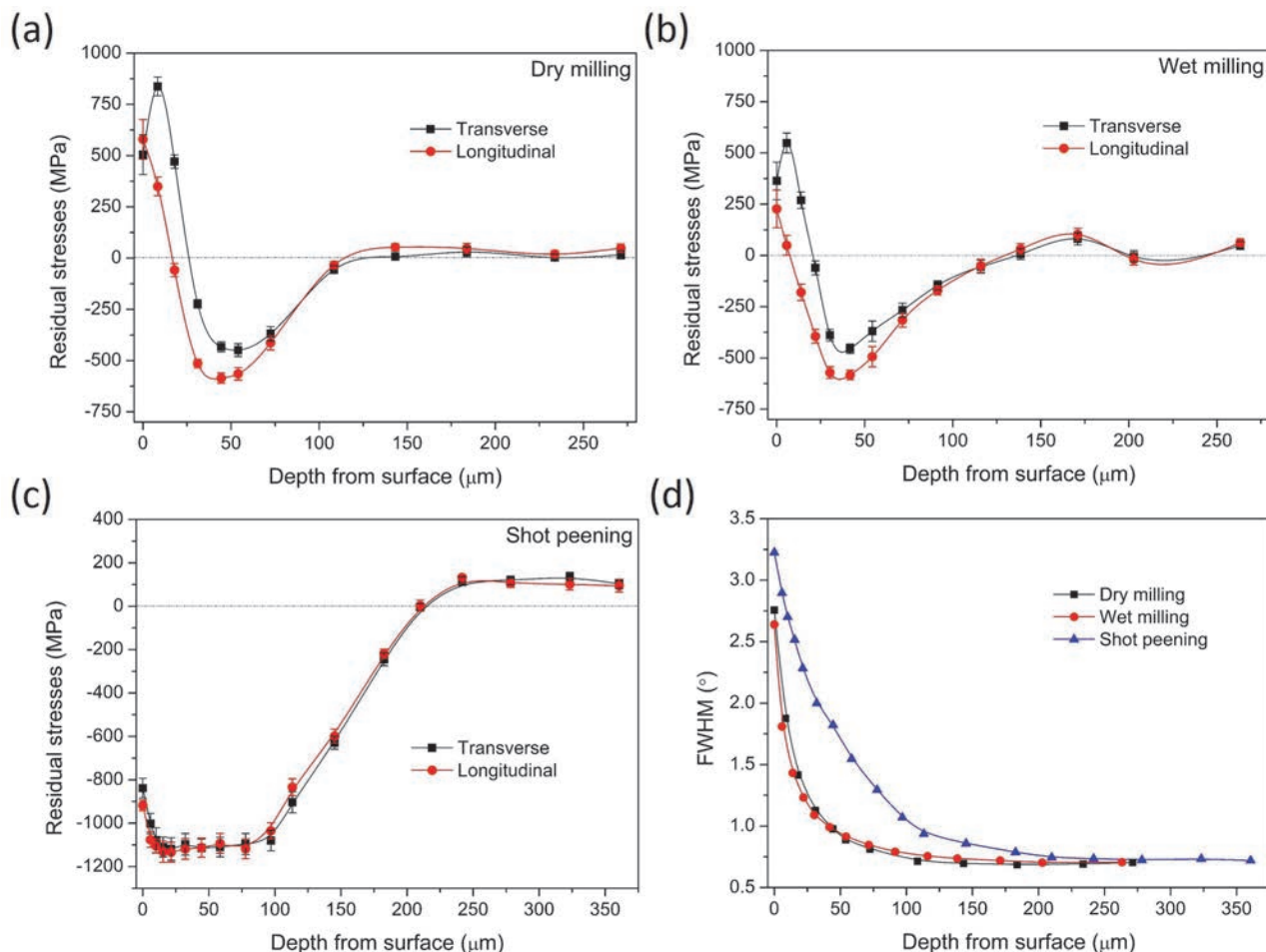
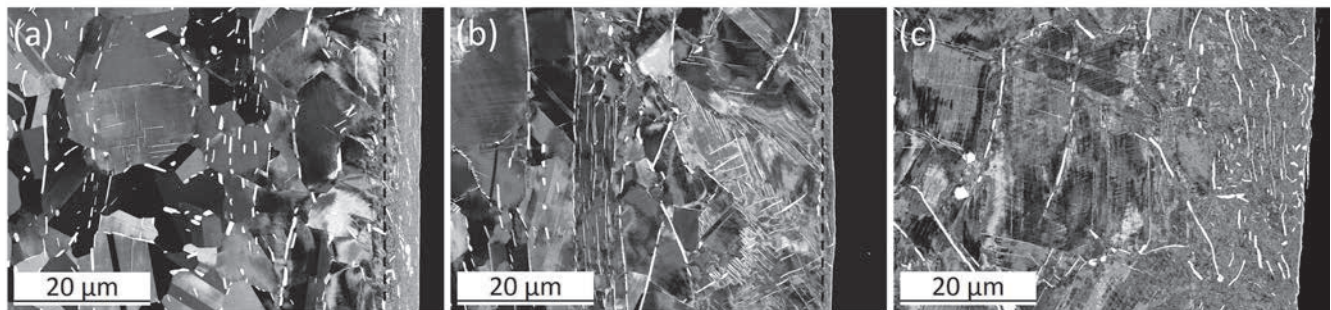


Figure 1. In-depth residual stresses generated by (a) dry milling, (b) wet milling, and (c) shot peening; (d) A comparison of the full width at half maximum intensity (FWHM) obtained from the measured diffraction peaks.

The post-milling surface treatment by shot peening annihilated the high tension on the dry-milled surface and introduced a surface plateau, extending to a depth of 100  $\mu\text{m}$ , with great compressive residual stresses in both TD and LD, see Fig. 1(c). The high level of surface compression was created as a consequence of the mechanically-induced plastic deformation during shot peening. This can be seen from the dramatically increased broadening of the diffraction peaks, i.e. full width at half maximum intensity (FWHM), measured in the shot-peened surface layer, see Fig. 1(d). The formation of the tensile residual stresses on the milled surface is most likely to be of thermal origin associated with the great heat generation during machining [1]. From Fig. 1(d), one can see that the wet-milled surface underwent less plastic deformation compared with that in the case of dry milling. A very likely explanation is that the coolant could contribute to lowering the friction and dissipating the generated heat, leading to a relatively low cutting temperature. As an effect of the reduced cutting temperature, the thermally-induced residual stresses became less in tension on the surface produced by wet milling. The

reduced thermal impact during wet milling can be further supported by the microstructural characterization beneath the milled surfaces. Instead of a continuous thick white layer, approximately 4 to 5  $\mu\text{m}$ , as observed on the dry-milled surface (Fig. 2(a)), the surface white layer appeared discontinuously with a thickness less than 1  $\mu\text{m}$  on the wet-milled surface (Fig. 2(b)). As suggested by Bushlya et al. [8], the development of white layers takes place in machining of Inconel 718 normally when the cutting temperature is increased, e.g. at high cutting speeds, cutting with worn tools or in dry machining operations. The shot-peened surface compared with the dry-milled surface showed significantly increased plastic deformation in microstructure, see Fig. 2(c), which is consistent with the greatly higher FWHM measured in the shot-peened layer.



*Figure 2. Electron channeling contrast imaging (ECCI) micrographs showing the microstructure beneath (a) the dry-milled surface, (b) the wet-milled surface, and (c) the shot-peened surface. In (a) and (b), dash lines are drawn to compare the thickness of the superficial white layer formed in dry and wet milling.*

A comparison of the fatigue performance as influenced by the use of coolant and post-machining surface treatment of shot peening is presented in Fig. 3. Although relatively low surface residual stresses were obtained by wet milling, the fatigue life was observed to be comparable with that for the specimens prepared by dry milling. However, in the high-cycle regime with a lower applied load, it showed a slight increase in fatigue resistance for the wet-milled condition which is very likely due to a stronger effect of residual stresses. The shot peening, on the other hand, led to a great increase of the fatigue life, particularly in the high-cycle regime; the enhancement could be up to roughly two orders of magnitude compared with the lifetime of the dry-milled specimens.

Fracture surface examinations can offer insights into the fatigue failure mechanism of the specimens with different surface conditions. Shown in Fig. 4 is an example of the typical fracture appearance observed on the fatigued specimens with either a dry-milled or wet-milled surface. It can be clearly seen that multiple cracks were initiated at the milled surface during fatigue loading and the coalescence of the cracks led to a macroscopic fluctuant fracture surface. Close examinations further revealed that the initiation of fatigue cracks took place primarily associated with the cracking of surface non-metallic inclusions (Nb-rich carbides and/or Ti-rich nitrides). Previous studies by the authors [9] have shown that the giant plastic work during machining of Inconel 718 could cause cracking of non-metallic inclusions on the machined surface. In this study, substantial cracked carbides as well as a few cracked nitrides (due to the much lower amount of nitrides in the alloy) were also observed after the milling operations. These pre-existing surface defects provide multiple sites where fatigue cracks preferably initiate, or could even start to grow without an incubation of nucleation. Based on such predominance of the failure mechanism, the comparable fatigue life of the specimens prepared by dry and wet milling is very likely attributed to the similar damage on the milled surfaces with respect to the non-metallic inclusion cracking. The effect of residual stresses in this case appears to be less significant.

In the case of the shot-peened specimens, the surface compression was deep and strong enough to shift the crack initiation sites to subsurface regions corresponding to the depth of the compressive layer, see Fig. 5. The surface microstructure of the shot-peened specimens still consists of a large amount of cracked inclusions, however, the development of fatigue cracks from these flaws was retarded due to the

presence of the great compressive residual stresses. As a result, an enhanced fatigue life and strength were obtained, as shown in Fig. 3. The beneficial effect of compressive residual stresses in terms of retarding surface cracking during fatigue and increasing the resistance of the component to fatigue failures is well consistent with the previous findings in shot peening of other metallic materials [3,4]. The extent to which the lifetime was prolonged was decreased as the applied load was increased due to the residual stress relaxation in low cycle fatigue resulting from significant cycling strains [10].

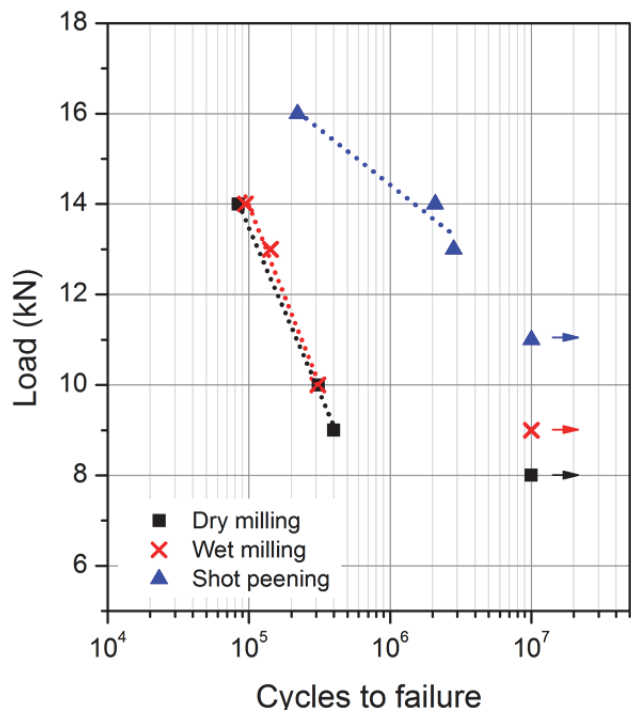


Figure 3. A comparison of the obtained fatigue life as influenced by the use of coolant as well as the post-machining surface treatment of shot peening.

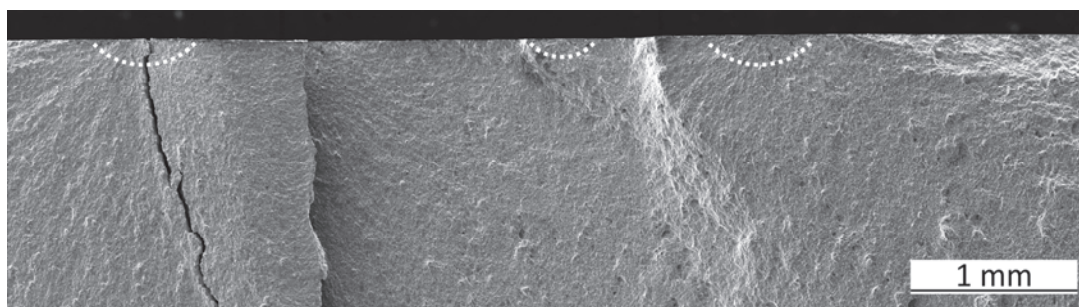


Figure 4. Typical fracture appearance after the fatigue of the milled specimens regardless of the use of coolant where multiple crack initiation sites at the milled surface were observed; some of them are located by dash lines.

### Conclusions

The present work investigated the residual stresses generated on milled Inconel 718 as influenced by the use of coolant in machining or by post-machining surface treatment with shot peening. The corresponding fatigue performance of the specimens was also investigated. The results showed that the wet milling led to reduced tensile residual stresses on the machined surface compared with that in the case of dry milling. However, a comparable fatigue life was obtained for the specimens milled with or without the use of the coolant. This is very likely due to that for both conditions the milling-induced surface damage with respect to cracked non-metallic inclusions dominated the crack initiation during fatigue. The shot-peening treatment annihilated the surface tension induced by milling and introduced high compressive residual stresses. The presence of the compressive layer retards surface cracking from the pre-existing cracked carbides and/or nitrides and shifts the crack initiation sites to sub-surface

regions, leading to a significant increase of the fatigue life and strength for the shot-peened specimens. The extent to which the lifetime was prolonged was reduced as the applied load was increased.

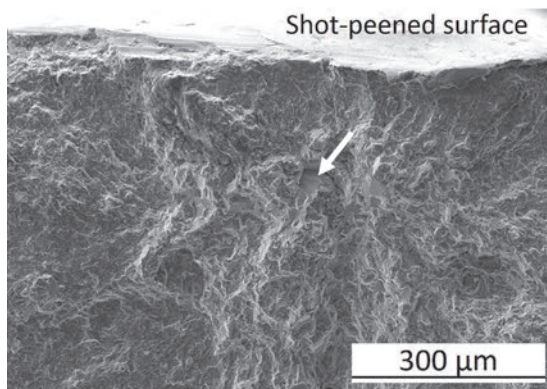


Figure 5. Fatigue fracture surface of a shot-peened specimen where it shows a transition of the crack initiation site from surface to subsurface regions (pointed by the arrow) compared with the observation in Fig. 4.

#### Acknowledgements

Faculty grant SFO-MAT-LiU#2009-00971 at Linköping University, Ytstruktur Arboga AB and Siemens Industrial Turbomachinery AB are acknowledged for their valuable supports in this study.

#### References

- [1] K. Jacobus, R. DeVor, S. Kapoor, Machining-induced residual stress: experimentation and modeling, *J. Manuf. Sci. Eng.* 122 (2000) 20-31.  
<http://dx.doi.org/10.1115/1.538906>
- [2] F. Pusavec, H. Hamdi, J. Kopac, I. Jawahir, Surface integrity in cryogenic machining of nickel based alloy-Inconel 718, *J. Mater. Process. Technol.* 211 (2011) 773-783.  
<http://dx.doi.org/10.1016/j.jmatprotec.2010.12.013>
- [3] J. Lindemann, C. Buque, F. Appel, Effect of shot peening on fatigue performance of a lamellar titanium aluminide alloy, *Acta Mater.* 54 (2006) 1155-1164.  
<http://dx.doi.org/10.1016/j.actamat.2005.10.043>
- [4] L. Wagner, Mechanical surface treatments on titanium, aluminum and magnesium alloys, *Mater. Sci. Eng. A* 263 (1999) 210-216.  
[http://dx.doi.org/10.1016/S0921-5093\(98\)01168-X](http://dx.doi.org/10.1016/S0921-5093(98)01168-X)
- [5] Y. Choi, A study on the effects of machining-induced residual stress on rolling contact fatigue, *Int. J. Fatigue* 31 (2009) 1517-1523.  
<http://dx.doi.org/10.1016/j.ijfatigue.2009.05.001>
- [6] A. Thakur, S. Gangopadhyay, State-of-the-art in surface integrity in machining of nickel-based super alloys, *Int. J. Mach. Tools Manuf.* 100 (2016) 25-54.  
<http://dx.doi.org/10.1016/j.ijmachtools.2015.10.001>
- [7] I.C. Noyan, J.B. Cohen, Residual stress-measurement by diffraction and interpretation, (1986).
- [8] V. Bushlya, J. Zhou, F. Lenrick, P. Avdovic, J. Ståhl, Characterization of white layer generated when turning aged Inconel 718, *Procedia Eng.* 19 (2011) 60-66.  
<http://dx.doi.org/10.1016/j.proeng.2011.11.080>
- [9] Z. Chen, R.L. Peng, J. Moverare, P. Avdovic, J. Zhou, S. Johansson, Surface integrity and structural stability of broached Inconel 718 at high temperatures, *Metall. Mater. Trans. A* 47 (2016) 3664-3676.  
<http://dx.doi.org/10.1007/s11661-016-3515-6>
- [10] R. McClung, A literature survey on the stability and significance of residual stresses during fatigue, *Fatigue Fract. Eng. Mater. Struct.* 30 (2007) 173-205.  
<http://dx.doi.org/10.1111/j.1460-2695.2007.01102.x>

## Effect of Ultrasonic Peening on Residual Stresses at a T-Butt Weld Toe

Alan K. HELLIER<sup>1,a \*</sup>, B. Gangadhara PRUSTY<sup>1,b</sup>, Garth M. PEARCE<sup>1,c</sup>,  
Mark REID<sup>2,d</sup>, Anna M. PARADOWSKA<sup>1,2,e</sup> and Peter SIMONS<sup>3,f</sup>

<sup>1</sup>School of Mechanical and Manufacturing Engineering, UNSW Australia, (The University of New South Wales), Sydney, NSW 2052, Australia

<sup>2</sup>Bragg Institute, Australian Nuclear Science and Technology Organisation (ANSTO), Lucas Heights, NSW 2234, Australia

<sup>3</sup>Applied Ultrasonics Australia, Suite 11/20 Narabang Way, Belrose, NSW 2085, Australia

<sup>a</sup>a.hellier@unsw.edu.au, <sup>b</sup>g.prusty@unsw.edu.au, <sup>c</sup>g.pearce@unsw.edu.au,  
<sup>d</sup>markr@ansto.gov.au, <sup>e</sup>anp@ansto.gov.au, <sup>f</sup>psimons@appliedultrasonics.com.au

**Keywords:** A350 Grade, Black Mild Steel Plate, T-Butt Welded Joint, Ultrasonic Peening, Residual Stresses, Fatigue Crack Growth, Parametric Equations

**Abstract.** The current paper presents the results of neutron diffraction measurements of the through-thickness residual stress field at the toe of a T-butt weld, made from 10mm thick A350 grade black mild steel plates, after successful ultrasonic peening. A single ultrasonic peening treatment was carried out at the weld toe. Residual stresses were measured using the KOWARI instrument at ANSTO. The neutron diffraction technique was chosen for this study because of its ability to measure three-dimensional residual stress deep within the component at high resolutions.

Although the nominal yield stress of the A350 grade plate is 350 MPa the actual yield stress is generally higher, in this case averaging out to about 400 MPa. Ultrasonic peening was highly effective, leading to a residual stress redistribution with a maximum compressive stress of about 250 MPa at the weld toe surface and a maximum tensile stress of 220 MPa, at a depth of almost 3mm into the base plate. The resulting compressive residual stresses at the weld toe surface will almost certainly increase substantially both the fatigue initiation and propagation lives, or may *prevent fatigue completely*. Since A350 steel is widely used in buildings, bridges and offshore structures, ultrasonic peening shows great promise as an in-situ peening method in order to improve weld fatigue performance.

### Introduction

A350 grade black mild steel is one of the most widely used structural materials in the world, being commonly found in buildings, bridges and offshore structures. Welding is typically used to join two plates of structural steel and this often takes the form of a T-butt weld. In addition, other more complex geometrical joints are often simplified for stress analysis purposes by approximating them as two-dimensional T-butt plate models (e.g. skewed T-joints, tubular welded joints, pipe-plate joints, etc.). However, all such welds are potentially susceptible to fatigue crack initiation and slow but accelerating growth arising as a result of fluctuating service loads, often eventually resulting in fast fracture.

Ultrasonic peening, more properly known as ultrasonic impact treatment (UIT), is a recent development of the well-established shot peening process. It was originally invented in 1972 in the former USSR to improve the fatigue and corrosion performance of ship and submarine hulls. UIT is similar to conventional needle or hammer peening in many respects. An important difference is that rather than using a pneumatic tool, which causes the needles or a single hammer-like rod to impact

the weld surface at a frequency of 25-100 Hz, with UIT, the weld is impacted by a small number of rods vibrating at a much higher frequency on the order of 18,000-27,000 Hz. This makes it a much quieter device, which vibrates at a lower intensity, so that the operator can use it for longer periods of time before tiring [1]. Ultrasonic peening is relatively cheap, can be applied in-situ and offers significant improvements in the lifespan of welded components when applied correctly. This occurs for three different reasons: removal of weld defects; reduction of stress concentration; and redistribution of tensile stresses and/or introduction of compressive stresses [2].

### Experimental Methods

**Welding.** Dimensions were 800×160×10mm for the base plate and 100×160×10mm for the attachment plate of each T-butt. During fabrication two base plates were tack welded back-to-back prior to welding of the double-beveled attachment plate to each, in order to minimize distortion. Balanced full-penetration GMAW fillet welding was employed, with six passes on each side. All welds passed ultrasonic testing (UT) for internal flaws and magnetic particle inspection (MPI) for surface flaws. Fig. 1 shows the weld detail of a typical T-butt joint before buffing.

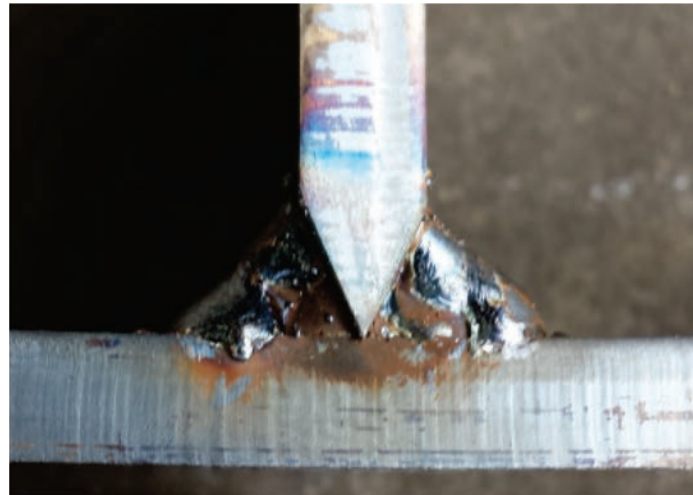


*Fig. 1. Weld detail of typical T-butt joint before buffing.*

**Ultrasonic Peening.** Ultrasonic peening treatments were carried out at the base plate and attachment plate weld toes on both sides of one of the T-butts using an Applied Ultrasonics Esonix UIT apparatus. The impact pins were oriented 45° from the treated weld area (perpendicular to the toe line) and the tool was continuously moved in an oscillating motion in a path parallel to the direction of the weld. In order to develop the desired groove, the tool was worked back and forth between a 30° and a 60° angle while maintain the oscillating motion described above. Groove formation was continuously observed during the application process. A properly formed, shiny groove at the weld toe was obtained; this is the main quality assurance inspection point for treatment verification [3].

**Neutron Diffraction.** It was attempted to measure through-thickness residual stresses from the weld toe into the base plate for both as-welded and ultrasonically peened specimens using the KOWARI instrument at the ANSTO Bragg Institute. The (non-destructive) neutron diffraction technique was chosen for this study because of its ability to measure three-dimensional residual stress deep within the component at high resolutions. For the neutron measurements a 0.5×0.5×1mm<sup>3</sup> gauge volume was used for the longitudinal, transverse and normal components. The experimental measurements on the ultrasonically peened sample were successful but those on the as-welded sample were unfortunately shown to be incorrect, as the scan was made slightly inside the weld rather than exactly at the weld toe.

**Parametric Equations.** Brennan-Dover-Karé-Hellier (BDKH) parametric equations [4] are available for the stress intensity factor (SIF) geometric Y-factor at the deepest point of a semi-elliptical flaw at the toe of a T-butt weld, accurate for a wide range of geometric parameters under both tension (membrane) and pure bending loadings. These were derived from the results of eighty 8-noded shell finite element analyses in conjunction with the Niu-Glinka weight function [5]. From the models studied, the geometry validity limits for the equations developed are:

Weld angle:	$30^\circ \leq \alpha \leq 60^\circ$	
Crack aspect ratio:	$0 \leq a/c \leq 1.0$	
Crack depth:	$0.01 \leq a/T \leq 1.0$	(1)
Weld toe radius:	$0.01 \leq \rho/T \leq 0.066$	
Attachment width:	$0.3 \leq L/T \leq 4.0$	

Fig. 2 shows the geometry of the T-butt weldments studied including the crack geometry, with all the geometric parameters above defined.

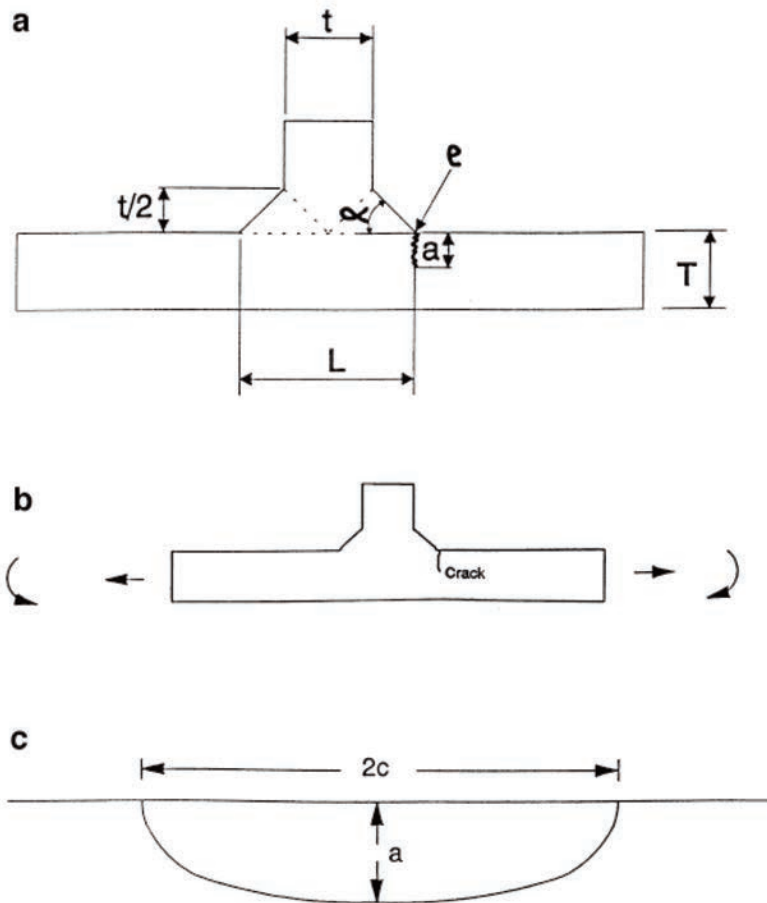


Fig. 2. (a) Local weld geometry studied (b) Geometry and loading used to derive stress intensity factors (c) Crack geometry (semi-elliptical crack).

Recently developed and unique Hellier-Brennan-Carr (HBC) T-butt weld toe surface stress concentration factor (SCF) [6] and stress distribution parametric equations [7] through the base plate thickness (i.e. the potential Mode I crack plane) are also available for similar ranges of geometric parameters and tensile (membrane) loading.

**Crack Growth Equations.** The Paris Law [8] is commonly used to predict the (Stage 2) fatigue propagation life for a component or structure containing a sharp initial crack. It does not take into

account the influence of mean stress. Another equation which does incorporate the (second order) influence of mean stress on the propagation rate is the Forman Equation [9].

**Computer Programs to Predict Fatigue Life.** Two FORTRAN computer programs were written to predict the remaining fatigue life for a T-butt welded joint containing a semi-elliptical crack at the weld toe under tension (membrane) loading. The first of these programs uses the BDKH tension parametric equation in conjunction with the Paris Law, and is applicable to a stress-relieved joint. The second program uses the BDKH tension parametric equation together with the HBC tension parametric equation and the Forman Equation, and is applicable to both the as-welded and ultrasonically peened conditions where residual stresses are present.

### Experimental Results

**Residual Stresses.** Although the nominal yield stress of the A350 grade plate is 350 MPa the actual yield stress is generally higher, in this case averaging out to about 400 MPa. Ultrasonic peening was highly effective, leading to a residual stress redistribution with a maximum compressive stress of about 250 MPa at the weld toe surface and a maximum tensile stress of 220 MPa, at a depth of almost 3mm into the base plate (refer to Fig. 3).

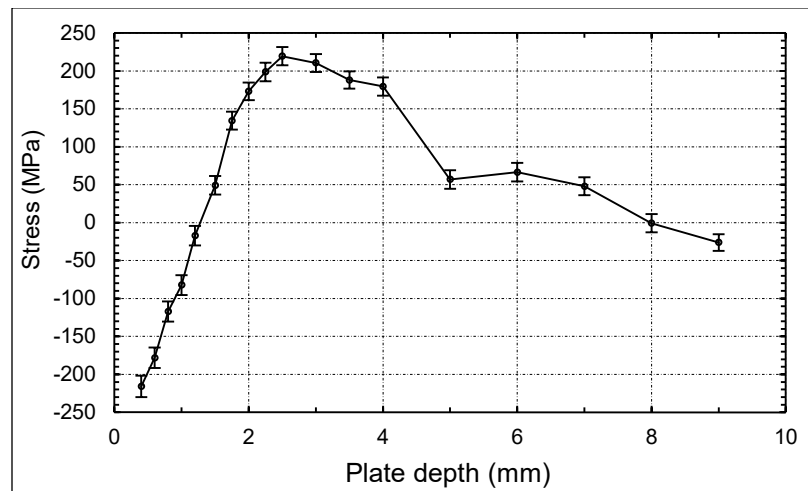


Fig. 3. T-butt weld toe residual stresses through the base plate after ultrasonic peening.

Since there are no measurements in the as-welded state, a typical as-welded residual stress distribution from the literature [10] was used instead, as shown in Fig. 4. The sample investigated using neutron diffraction with a  $2 \times 2 \times 2 \text{ mm}^3$  gauge volume was a T-plate fillet weld, joining two 25mm thick plates. The plate material was BS 7191 grade 355 EMZ structural steel, which is very similar to A350 grade steel, and represents a large group of steels commonly used in the nuclear and offshore industries. SMAW welding with standard filler metal was used. Both welds consisted of four weld passes in an alternating sequence between the two sides. For the purpose of this work, the residual stress distribution at the T-butt weld toe centre line was scaled horizontally to fit a 10mm thick base plate.

**Geometric, Material and Loading Parameters.** Table 1 contains values of the geometric parameters selected for the present analyses.

The fatigue threshold,  $\Delta K_{\text{th}}$ , was taken as  $3.2 \text{ MPa}\sqrt{\text{m}}$ . The Paris Law crack growth coefficient and exponent were  $C = 8.57 \times 10^{-12}$  (SI units) and  $m = 3$ , respectively. Applied membrane stress varied from 0 to 100 MPa. The number of crack increments employed in the modelling was 10,000.

**Preliminary Results.** Fig. 5 shows the numerical crack growth results superimposed for: (a) as-welded; (b) stress-relieved; and (c) ultrasonically peened conditions. The analyses conducted assumed that a fatigue crack grows through a static residual stress field. As expected, it is apparent

that the ultrasonically peened T-butt exhibited a longer fatigue life than the stress-relieved specimen, which in turn had a longer fatigue life than the as-welded specimen. It should be noted that the ultrasonically peened specimen had an initial crack depth of 1mm; when it had the same 0.1mm initial crack depth as the other two specimens it exhibited *no fatigue crack growth at all*.

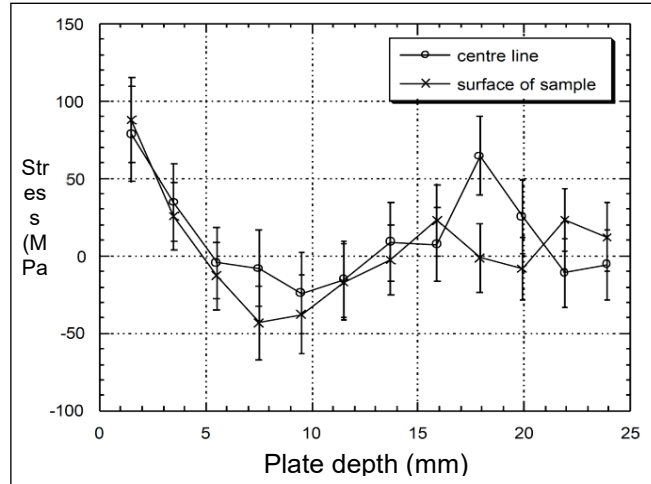


Fig. 4. Through-thickness residual stresses at T-butt weld toe centre line and surface of the sample as a function of base plate depth [10].

Table 1. Geometric parameters of T-butt joints.

Geometric Parameter	Value
Weld angle [ $\alpha$ ]	45°
Weld toe radius [ $\rho$ ]	0.1mm
Plate thickness [ $T$ ]	10mm
Welded attachment width [ $L$ ]	30mm
Initial semi-elliptical crack depth [ $a_i$ ]	0.1mm or 1mm
Initial semi-elliptical crack width [ $2c_i$ ]	2mm or 20mm

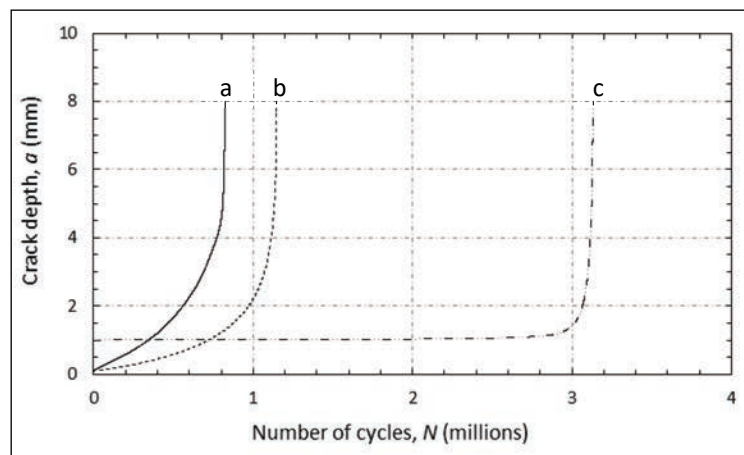


Fig. 5. Fatigue crack growth curves (a) As-welded (b) Stress-relieved (c) Ultrasonically peened specimens.

**Conclusions**

Ultrasonic peening was found to be very effective at modifying the residual stress distribution. As expected the as-welded residual stresses shortened the fatigue propagation life, whereas ultrasonic peening extended it or *completely prevented fatigue crack growth*.

## References

- [1] R.T. Yekta, S. Walbridge, Acceptance Criteria for Ultrasonic Impact Treatment (UIT), Ontario Ministry of Transportation, Provincial Highways Management Division, Highway Infrastructure Innovation Funding Program, Final Report No. HIIFFP-110, Canada, February 2013.
- [2] L. Lopez Martinez, Z. Barsoum, A. Paradowska, State-of-the-art: Fatigue life extension of offshore installations, in: Proc. 31st International Conference on Ocean, Offshore and Arctic Engineering (OMAE2012), Rio de Janeiro, Brazil, 1-6 July 2012, Paper 83044.  
<http://dx.doi.org/10.1115/omae2012-83044>
- [3] Esonix UIT, Application Guide, Post Weld Treatment for Fatigue Enhancement, Carbon Steel Welded Structures, Applied Ultrasonics, Revision 2.0, Revision Date: 28 June 2006.
- [4] F.P. Brennan, W.D. Dover, R.F. Karé, A.K. Hellier, Parametric equations for T-butt weld toe stress intensity factors, Int. J. Fatigue 21 (1999) 1051-1062.  
[http://dx.doi.org/10.1016/S0142-1123\(99\)00090-0](http://dx.doi.org/10.1016/S0142-1123(99)00090-0)
- [5] X. Niu, G. Glinka, Theoretical and experimental analyses of surface fatigue cracks in weldments, in: W.G. Reuter, J.H. Underwood, J.C. Newman (Eds.), Proc. Symposium on Surface-Crack Growth: Models, Experiments, and Structures, Sparks, NV, 25 April 1988, ASTM STP 1060, American Society for Testing and Materials, Philadelphia, PA, 1990, pp. 390-413.  
<http://dx.doi.org/10.1520/stp23445s>
- [6] F.P. Brennan, P. Peleties, A.K. Hellier, Predicting weld toe stress concentration factors for T and skewed T-joint plate connections, Int. J. Fatigue 22 (2000) 573-584.  
[http://dx.doi.org/10.1016/S0142-1123\(00\)00031-1](http://dx.doi.org/10.1016/S0142-1123(00)00031-1)
- [7] A.K. Hellier, F.P. Brennan, D.G. Carr, Weld toe SCF and stress distribution parametric equations for tension (membrane) loading, in: Proc. Fatigue 2014, 11th International Fatigue Congress, MCG, Melbourne, 2-7 March 2014, Adv. Mater. Research 891-892 (2014) 1525-1530.
- [8] P. Paris, F. Erdogan, A critical analysis of crack propagation laws, Trans. ASME, J. Basic Eng. 85 (1963) 528-534.  
<http://dx.doi.org/10.1115/1.3656900>
- [9] R.G. Forman, V.E. Kearney, R.M. Engle, Numerical analysis of crack propagation in cyclic-loaded structures, Trans. ASME, J. Basic Eng. 89 (1967) 459-463.  
<http://dx.doi.org/10.1115/1.3609637>
- [10] P.S. May, R.C. Wimpory, G.A. Webster, N.P. O'Dowd, Determination of the Residual Stress Distribution in a Welded T-Plate Joint, Experimental Report, REST Instrument, Experiment Number 425, The Studsvik Neutron Research Laboratory (NFL), University of Uppsala, Studsvik, Sweden, 2000.

## Structural Engineering Studies on Reinforced Concrete Structure using Neutron Diffraction

Hiroshi Suzuki<sup>1,a,\*</sup>, Koichi Kusunoki<sup>2,b</sup>, Manabu Kanematsu<sup>3,c</sup>, Tomohisa Mukai<sup>4,d</sup>  
and Stefanus Harjo<sup>5,e</sup>

<sup>1</sup> Materials Sciences Research Center, Japan Atomic Energy Agency, Tokai, Naka, Ibaraki, Japan

<sup>2</sup> Earthquake Research Inst., Univ. of Tokyo, Bunkyo-ku, Tokyo, Japan

<sup>3</sup> Dept. of Architecture, Tokyo Univ. Sci., Noda, Chiba, Japan

<sup>4</sup> Department of Structural Engineering, Building Research Inst., Tsukuba, Ibaraki, Japan

<sup>5</sup> J-PARC Center, Japan Atomic Energy Agency, Tokai, Naka, Ibaraki, Japan

<sup>a</sup>suzuki.hiroshi07@jaea.go.jp, <sup>b</sup>kusunoki@eri.u-tokyo.ac.jp, <sup>c</sup>manabu@rs.noda.tus.ac.jp

<sup>d</sup>t\_mukai@kenken.go.jp, <sup>e</sup>stefanus.harjo@j-parc.jp

**Keywords:** Neutron Diffraction, Reinforced Concrete, Transverse Rib, Bond Stress

**Abstract.** It has been demonstrated in our past studies that neutron diffraction can be an alternative method to conventional strain gauges for measuring the stress distribution along rebar embedded in concrete. The current study investigated the possibility of the bond stress evaluation using neutron diffraction in order to find a further capability of neutron diffraction for the structural engineering study on the reinforced concrete structure. Several peaks appeared in the bond stress distribution measured by neutron diffraction, showing the inhomogeneous bond variation along the embedded rebar. This result suggests that the neutron diffraction technique with high spatial resolution makes it possible to investigate local bond resistance caused by the transverse ribs. The bond stress distribution measured by the neutron diffraction technique is expected to bring detailed understanding of the bond mechanism between rebar and concrete for the reinforced concrete structure.

### Introduction

The reinforced concrete (RC), which is widely utilized for various architectural and civil engineering structures, is well known as a composite structure, in which concrete with relatively low tensile strength and ductility is strengthened by reinforcements such as steel rods (rebars) with high tensile strength and/or ductility. In general, quantitative evaluation of bond resistance between rebar and surrounding concrete is important to discuss the performance of the RC structures [1-4]. In our previous studies, we have investigated the potential of the neutron diffraction technique for the stress measurement of rebar embedded in concrete as an alternative method to the conventional strain gauge. Our first relevant work was carried out using the engineering diffractometer RESA-1 in JRR-3 (Japan Research Reactor No. 3), and we demonstrated that the neutron diffraction technique can be a novel strain measurement method for rebar embedded in concrete [5, 6]. More recently, three-dimensional deformation behavior of the embedded rebar including the axial and transverse strains was successfully measured under pull-out loading using Time-of-Flight (TOF) neutron diffraction with the engineering diffractometer, TAKUMI in MLF (Materials and life Science Experimental Facility) of J-PARC (Japan Proton Accelerator Research Complex) [7]. Furthermore, it was demonstrated by some application studies using TAKUMI that the neutron diffraction technique is available to assess the bond deterioration due to rebar corrosion and crack generation in concrete [8]. As described above, our previous studies commonly discussed on the bond condition between rebar

and concrete based on a change in the axial stress distributions along the embedded rebar measured by neutron diffraction. However, most of the papers investigating the bond strength for the RC structures have rather discussed on a change in the “bond stress distribution” rather than the axial stress distribution [9, 10].

The current study was, therefore, undertaken to evaluate the bond condition of the RC structure based on the bond stress distribution along the embedded rebar, in order to find further capability of neutron diffraction for the structural engineering study of the RC structure.

### Experimental Procedure

**RC Specimens.** Figure 1 (a) shows a schematic illustration of the RC specimen used in this study. A ferritic steel deformed-bar with 9.53 mm in a nominal diameter, so-called D10 rebar, was embedded in cylindrical concrete with approximately 50 mm in diameter and 460 mm in length. The length of the bonded region is 320 mm, and an un-bonded region with 110 mm in length was artificially introduced at the loading edge of the specimen. This un-bonded region was utilized for determining the reference lattice parameter with stress-free condition. The boundary between bonded and un-bonded regions was defined as the origin of length scale ( $X=0$ ). The maximum size of the mixed aggregates in the concrete was 13 mm in diameter. This specimen was cured in air for total 29 days before the neutron experiment, i.e. first 14 days at ambient condition and last 15 days in a constant temperature ( $20\pm 1$  °C) and humidity ( $60\pm 5$  RH%) room. The compressive and tensile strengths of concrete cured in air for 50 days under the same condition as the reinforced concrete specimen were measured as a reference to be 34.6 MPa and 2.79 MPa, respectively. The specimen was mounted on the pull-out loading device which consists of a hydraulic center-hole jack, a center-hole load cell and coil spring, as shown in Fig. 1 (b).

**Neutron Experiment.** The engineering diffractometer, TAKUMI [11], installed at BL19 in MLF of J-PARC was employed in this study. Figure 1 (c) shows the schematic layout of TAKUMI for the stress measurement of rebar embedded in concrete. This is an energy dispersive neutron engineering diffractometer, which measures energy spectrum diffracted from a sample when irradiating with white pulsed neutrons at 25 Hz generated in the mercury target. The incident neutron beam was formed into a rectangular shape with 5 mm in width and 10 mm in height by using a gauge definition slit, irradiating the reinforced concrete specimen mounted on the loading device settled on a XYZ $\theta$  positioner. The specimen with the loading device was oriented 45° to the incident beam, and therefore allowed us to measure the strains of rebar in the axial and transverse directions simultaneously using both detector banks installed at  $\pm 90^\circ$ . The radial collimators for 5 mm gauge width were installed in front

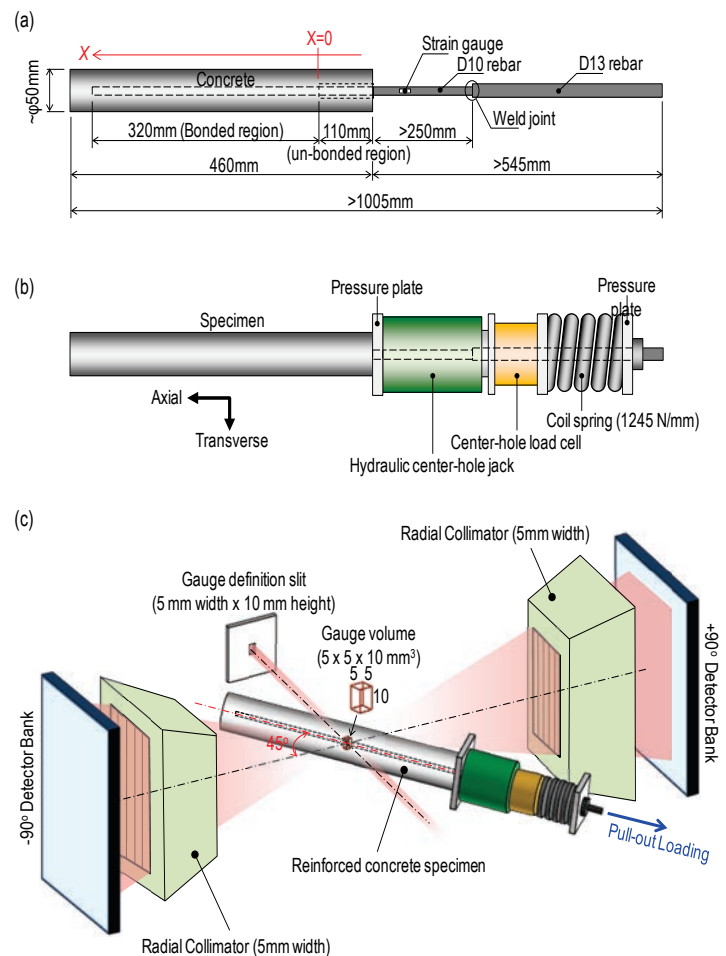


Fig. 1 Schematic illustrations of (a) sample used in this study, (b) load frame and (c) measurement configuration of TAKUMI.

of each detector bank, resulting in the gauge volume of  $5 \times 5 \times 10 \text{ mm}^3$ . The diffraction patterns were measured at 5 mm intervals in minimum along rebar over the length of 250-300 mm including the first 50 mm un-bonded region under different pull-out loadings, i.e. approximately 125 MPa and 248.5 MPa. The detailed descriptions of the experimental condition including the sample preparation can be found in the reference [7].

**Data Analysis.** The average lattice constants,  $a$  in the axial and transverse directions were determined by multiple-fitting over 15 peaks from the 110 to 431 reflections by the Rietveld refinement software, Z-Rietveld [12]. The axial stress in a rebar axis,  $\sigma_A$  was calculated using the strains in the axial and transverse directions of rebar in assumption of equiaxial-stress condition [7]. On the other hand, the bond stress,  $\tau$  is equivalent to the shear stress acting at the boundary between rebar and concrete, expressed by following equation,

$$\tau = \frac{A}{\pi D} \cdot \left| \frac{d\sigma_A}{dX} \right| = \frac{D}{4} \cdot \left| \frac{d\sigma_A}{dX} \right|, \quad (1)$$

where,  $A$  and  $D$  indicate a nominal cross-sectional area and a nominal diameter of rebar, respectively. According to Eq (1), the bond stress distribution can be obtained by making a differential curve of the axial stress distribution. In this study, the binomial smoothing was, at first, applied to the measured axial stress distribution to reduce the influence of data scattering, and then the bond stress distribution was obtained by plotting slopes fitted within a range of neighboring data in the smoothed axial stress distribution, as a function of the axial position of rebar.

The average bond stress was, in our previous studies [5-8], roughly calculated by Eq (1) with the slope of the axial stress distribution within a range of the anchorage region, approximately estimated by eye. In contrast, it was obtained accurately in this study normalizing the area of the bond stress diagram in the anchorage region by its length.

### Results and Discussion

Figure 2 shows the axial stress distributions and corresponding bond stress distributions along the embedded rebar in concrete under two different pull-out loadings, i.e.  $\sigma_{ap}=125 \text{ MPa}$  and  $248.5 \text{ MPa}$ . Figure 2(a) exhibits the axial stress distribution with a spatial resolution of 5 mm in minimum, showing typical stress variation for the RC structure under pull-out loading as an increase in the tensile stress towards the end of the bonded region ( $X=0 \text{ mm}$ ). In addition, compressive residual stresses generated due to drying shrinkage of concrete can be found in the bonded region. The bond stress distribution derived from the smoothed axial stress distribution is shown in Fig. 2(b). Lengths of the anchorage region can be predicted to be about 85 mm for  $\sigma_{ap}=125 \text{ MPa}$  and about 145 mm for  $\sigma_{ap}=248.5 \text{ MPa}$ , and the average bond stresses are calculated to be about 6.4 MPa and 5.9 MPa, respectively. These values are different from rough estimation in our previous study [7], but more reliable since the bond stress distribution obtained here assists to determine these values accurately. On the other hand, several peaks can be

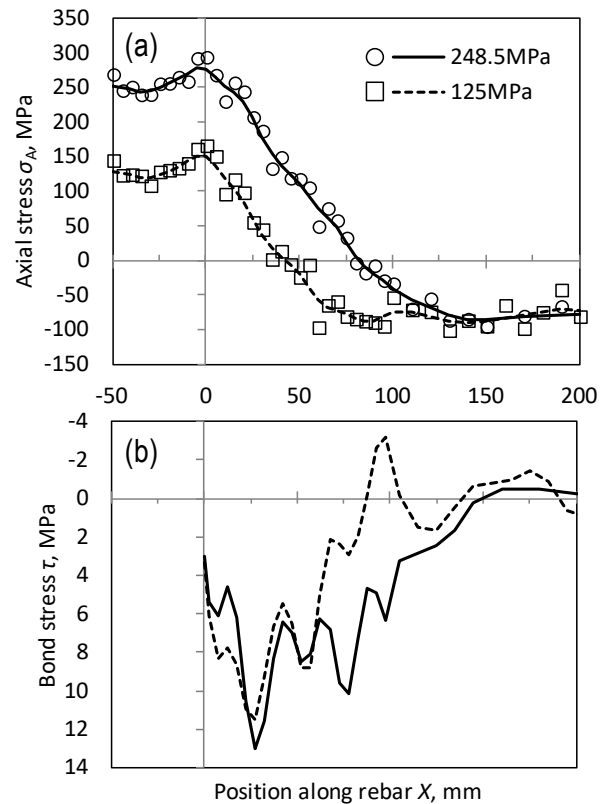


Fig. 2 (a) Axial stress and (b) bond stress distributions with 5 mm in spatial resolution. Average error bar of the measured axial stresses is  $\pm 22 \text{ MPa}$ .

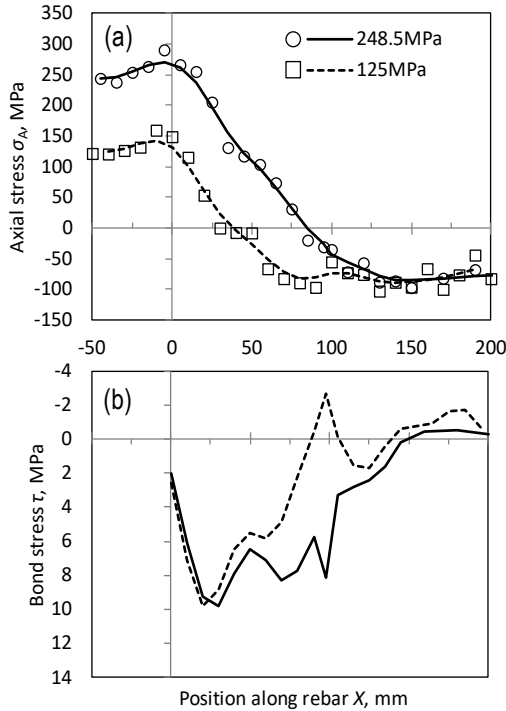


Fig. 3 (a) Axial stress and (b) bond stress distributions with 10 mm in a spatial resolution.

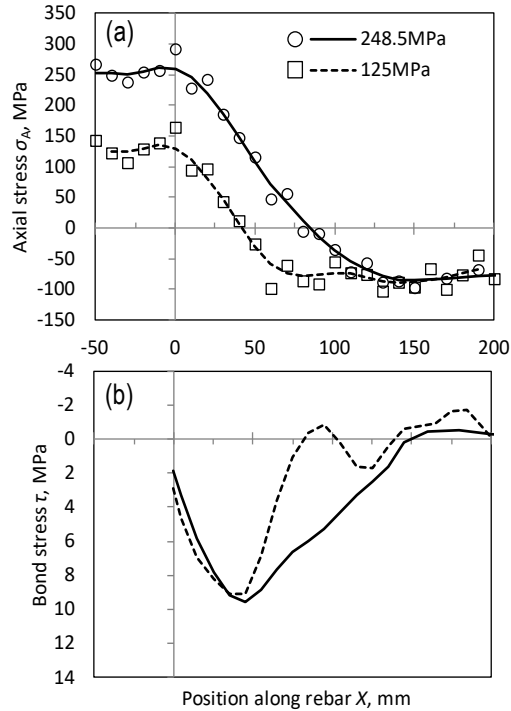


Fig. 4 (a) Axial stress and (b) bond stress distributions with 10 mm in spatial resolution, but it is 5mm offset from that in

found in the bond stress distribution with about 20 mm in intervals. Since the error bars of the bond stresses are estimated to be more than  $\pm 10$  MPa, the oscillations in Fig. 2(b) is suspected to be given by the scatter in the axial stresses. However, the cyclic variation showing similar pattern regardless of the applied stresses may be rather associated with ribs regularly distributed along rebar. To know the reason why several peaks appear in the bond stress distribution, therefore, following discussions are made based on the geometrical relationship between the transverse rib and measurement positions.

Figure 3 (a) shows the axial stress distribution with 10 mm in a spatial resolution, extracted from the original axial stress distribution shown in Fig. 2(a). The bond stress distribution obtained here looks similar pattern to the variation of Fig. 2(b), but showing some broader peaks. The average bond stresses are calculated to be about 5.8 MPa for both applied stresses, which are slightly smaller than those derived from the bond stress distribution with 5 mm in a spatial resolution. On the other hand, Fig. 4 (a) shows the axial stress distribution with the same spatial resolution of 10 mm, but it is 5mm offset from that in Fig. 3(a). As shown in Fig. 4(b), the bond stress distribution derived from the axial stress distribution has no peaks, which is clearly different from the variations shown in Figs. 2(b) and 3(b). The average bond stresses are calculated to be about 5.8 MPa for  $\sigma_{ap}=125$  MPa and about 5.6 MPa for  $\sigma_{ap}=248.5$  MPa, which are similar value to those in former case with 10 mm in a special resolution. Comparing the average bond stresses for all cases with different special resolutions, it can be confirmed that they agree within less than 1.0 MPa, regardless of the special resolution.

The results showing different trend of the bond stress distribution can be explained by the position relationship between the transverse ribs and measurement positions, as represented in Fig. 5(a). The distance between transverse ribs of D10 rebar is approximately 6.7 mm. If the rib position coincides with the measurement position at  $X=10$  mm, they are approximately overlapped every 20 mm when measuring the axial stress distribution with 5 mm in a spatial resolution, as shown in (i) in Fig. 5(a). Simply assuming a step-like axial stress distribution along the embedded rebar, the axial stress

distribution measured with 5 mm in a spatial resolution can be represented by the red line in the bottom figure of Fig. 5(a). In this case, unchanged flat variation can be observed every 20 mm, which brings a decrease in the bond stresses at corresponding positions. This simple model can approximately demonstrate the bond stress distribution shown in Fig 2(b). On the other hand, if the stress distribution is measured with 10 mm in a spatial resolution starting from  $X=5$  mm, the measurement positions cannot be overlapped with the rib positions at all (see (ii) in Fig. 5). In this case, the axial stress distribution fluctuates every 10 mm, showing similar trend to the case (i) in Fig. 5(a) but lower resolution, resulting in broader peaks in the bond stress distribution as shown in Fig. 3(b). If starting measurement from  $X=0$  mm with 10 mm in a spatial resolution, on the other hand, the measurement positions can be overlapped with another ribs every 20 mm, as shown in (iii) in Fig. 5. In this case, the axial stress distribution behaves similar trend to the case (ii) in Fig. 5(a), but seems to be shifted by 5 mm. Therefore, the bond stress distribution in Fig. 4(b) shows slightly different from that in Fig. 3(b). Considering above mechanisms, neutron diffraction can investigate local bond resistance taking advantage of higher spatial resolution than the strain gauge method. According to Fig. 5(b), the horizontal bearing force,  $F_H$  on the rib face is estimated to be smaller than the friction force,  $f_H$  on a straight part of rebar because of higher axial restriction of deformation around the transverse rib by the surrounding concrete. Therefore, lower and higher bond stresses in Fig. 2(b) are considered to be derived from the friction force,  $f_H$  and the horizontal bearing force,  $F_H$ , respectively.

**Summary**

In the present study, the capability of the neutron diffraction technique for the structural engineering studies on the reinforced concrete structure was discussed based on the bond stress evaluation between rebar and concrete. Several peaks appear in the bond stress distribution measured by neutron diffraction, showing the inhomogeneous bond variation along the embedded rebar. The horizontal bearing force on the rib face might increase the bond resistance around the transverse ribs, increasing

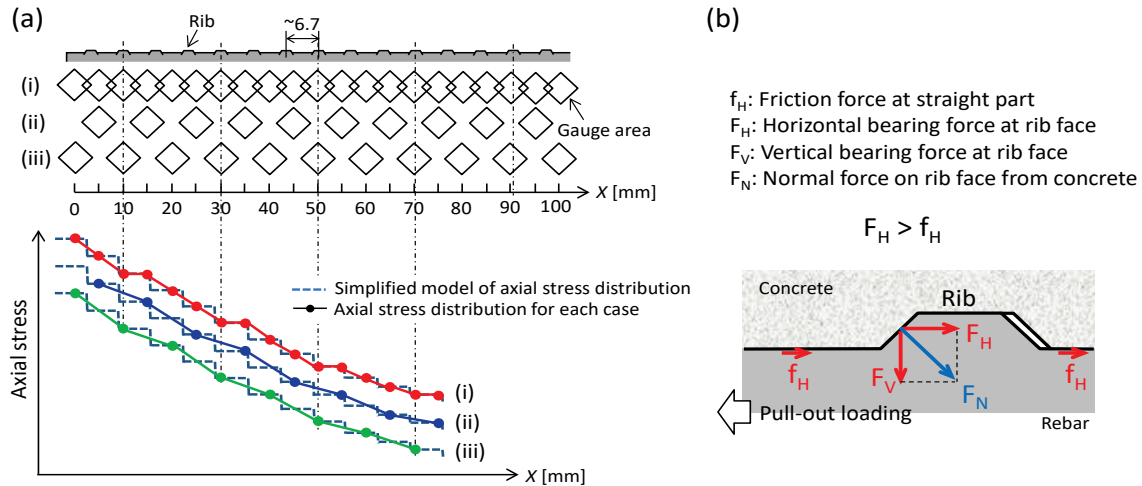


Fig. 5 (a) Schematic relationship between transverse rib and measurement positions and schematic diagram of the axial stress distribution estimated for each spatial resolution. (b) Schematic illustration of force working around a transverse rib.

the bond stresses locally. On the other hand, lower bond stresses are considered to be derived from weaker friction force acting at the straight part of rebar between transverse ribs. This result suggests that neutron diffraction technique with high spatial resolution can investigate local bond resistance caused by the transverse ribs. The bond stress distribution measured by the neutron diffraction technique is expected to bring detailed understanding of the bond mechanism between rebar and concrete for the reinforced concrete structures.

The absorption coefficient of concrete is approximately  $0.5 \text{ cm}^{-1}$  which is about a half of iron one [5]. For the future, to use deuterated concrete would decrease the transmission and allow higher spatial resolution and allow us to see more detailed cyclic variation associated with the ribs.

The neutron diffraction experiments were performed using the TAKUMI engineering diffractometer at the J-PARC/MLF with the approval of the J-PARC Center as Proposal No. 2012B0058.

## References

- [1] Y. Goto, Cracks formed in concrete around deformed tension bars, *ACI Journal*, 68 (1971) 244-251.
- [2] A. H. Nilson, Internal measurement of bond slip, *J. Am. Concr. Inst.*, 69 (1979) 439-441.
- [3] R. Tepfers, Cracking of concrete cover along anchored deformed reinforcing bars *Magazine of Concrete Research* 31 (1979) 3-12.  
<http://dx.doi.org/10.1680/mac.1979.31.106.3>
- [4] M. N. S. Hadi, Bond of high strength concrete with high strength reinforcing steel, *The Open Civil Engineering Journal*, 2 (2008) 143-147.  
<http://dx.doi.org/10.2174/1874149500802010143>
- [5] H. Suzuki, M. Kanematsu, K. Kusunoki, Neutron diffraction studies on strain evaluation of rebar in reinforced concrete, *Powder Diffraction*, 24, Issue S1 (2009) S68-S71.
- [6] K. Kusunoki, K. Kabayama, T. Mukai, Y. Hatanaka, H. Suzuki, A. Tasai, Experimental study on bonding action with neutron diffraction technique, *8CUEE CONFERENCE PROCEEDINGS*, (2011) 701-705.
- [7] H. Suzuki, K. Kusunoki, Y. Hatanaka, T. Mukai, A. Tasai, M. Kanematsu, K. Kabayama, S. Harjo, Measuring strain and stress distributions along rebar embedded in concrete using time-of-flight neutron diffraction, *Measurement Science and Technology*, 25 (2014) 025602.  
<http://dx.doi.org/10.1088/0957-0233/25/2/025602>
- [8] H. Suzuki, K. Kusunoki, M. Kanematsu, A. Tasai, Y. Hatanaka, N. Tsuchiya, S.C. Bae, S. Shiroishi, S. Sakurai, T. Kawasaki, S. Harjo, Application of neutron stress measurement to reinforced concrete structure, *JPS Conference Proceedings*, 8 (2015) 031006.  
<http://dx.doi.org/10.7566/jpsc.8.031006>
- [9] F. I. Faiyadh, Bond characteristics of oil saturated concrete, *Int. J. Cement Composites and Lightweight Concrete*, 7 (1985) 115-131.  
[http://dx.doi.org/10.1016/0262-5075\(85\)90067-3](http://dx.doi.org/10.1016/0262-5075(85)90067-3)
- [10] S. W. Lee, K. H. Tan, E. H. Yang, Bond-slip response of reinforcing bars embedded in high performance fiber reinforced cement composites, *Int. J. Civil Environmental, Structural, Construction and Architectural Engineering*, 9 (2015) 626-631.
- [11] S. Harjo, T. Ito, K. Aizawa, H. Arima, J. Abe, A. Moriai, T. Iwahashi, T. Kamiyama, Current status of engineering materials diffractometer at J-PARC, *Materials Science Forum*, 681 (2011) 443-448.  
<http://dx.doi.org/10.4028/www.scientific.net/MSF.681.443>
- [12] R. Oishi, M. Yonemura, Y. Nishimaki, S. Torii, A. Hoshikawa, T. Ishigaki, T. Morishima, K. Mori, T. Kamiyama, Rietveld analysis software for J-PARC, *Nuclear Instruments and Methods, A* **600** (2009) 94-96.

# Stress Analysis of the Bi-Metallic Coins – a Potential Shrink Fit Ring & Plug Standard

Scott Olsen<sup>1, a\*</sup>, Vladimir Luzin<sup>1, b</sup>

<sup>1</sup> Australian Nuclear Science and Technology Organisation, Locked Bag 2001, Kirrawee DC, NSW, 2232 Australia

<sup>a</sup> [sol@ansto.gov.au](mailto:sol@ansto.gov.au), <sup>b</sup> [vl@ansto.gov.au](mailto:vl@ansto.gov.au)

**Keywords:** Residual Stress, Neutron Diffraction, Bi-Metallic Coin

**Abstract.** The “Shrink-fit ring and plug” system is known in the residual stress neutron community mostly due to the VAMAS Round Robin specimens, that were measured by most of the neutron residual stress instruments worldwide. This standard, however, can be challenging for some low flux instruments and considerable beamtime and efforts are required to accomplish measurements accordingly to the measurement protocol. Theoretically, the residual stress distribution is not simple, being neither plain stress nor plain strain, and essentially it is a 3D distribution with a large gradient toward the flat cut, especially for the axial component. Another “shrink-fit ring-and-plug” system is being considered, namely bi-metallic coins. With an easier zero plane stress state, they represent another potential candidate for a standard. Bi-metallic coins are in current circulation in many countries of the world. In the given study we report on an assessment of the residual stress state of 7 different bi-metallic coins measured by means of neutron diffraction to reconstruct the full stress state. The magnitudes of the stresses in the specimens were different obviously due to differences in the coinage process and materials in use. While in some cases residual stresses are weak and therefore difficult to measure accurately, in some cases stresses reach ~100 MPa. Although question in variability of the coinage process through years and within series is still debatable, tight standards and tolerances of the mint industry suggest the probability of consistency in the residual stress state making bi-metallic coin an interesting alternative to the VAMAS ring-and plug standard..

## Introduction

The so-called VAMAS shrink-fit “ring-and-plug” sample [1] has been used over the last decade as a standard round-robin sample by the neutron community for the purpose of standardization and instrument calibration. The idea was so successful that all existing, newly built, or upgraded stress scanners made measurements of this sample, usually during commissioning. Collected data is commonly among the very first results, as in the case of residual stress diffractometer KOWARI at ANSTO [2]. Despite this success, there were few drawbacks with this approach:

- There were only two samples made and although they can become available within reasonable time, the associated logistics and mailing samples around the world without risk of losing them is problematic.
- Although aluminium barely activates during a normal neutron diffraction experiment (transmission tomography can be different!) moving samples that have been irradiated across borders can be problematic.
- The samples were produced in one single and unrepeated process, there is a seriously challenging problem if someone wishes to reproduce them exactly; there were some unsuccessful attempts in the past to make copies.

There are also problems of a scientific nature and related to the experimental process:

- The samples are made of aluminium alloy AA7050. Although this has the advantage of providing high penetration and low stiffness, both good for neutron strain measurements, aluminium is a weak scatterer, therefore for some residual stress diffractometers with moderate performance it is a challenging task to carry out the prescribed measurement programme in full. As a consequence

incomplete data sets were collected on some instruments, while on other beamlines spatial resolution or accuracy was sacrificed to have measurements done within reasonable experimental time.

- Another drawback of AA7050 alloy is that it is anisotropic and special efforts must be made to keep it under control and separate measurements of a specially made  $d_0$  sample (a stand-alone plug sample) should be performed slowing down the overall experiment.
- With overall dimensions 50 mm diameter and 50 mm height, the residual stress state is not simple, neither plane-strain state, nor plane stress state. In general, a gradient along the axis of the cylinder is present for strains and stresses. It is especially pronounced for the axial stress component which changes from a maximum value in the mid-height to exact zero at the top and bottom surfaces. Thus, results of the measurements, in principle, depend on the experimental setup and how measurements were executed, e.g. on the exact shape and size of the gauge volume

In an attempt to overcome these drawbacks, a much simpler standard sample can be envisaged. It should be made of a better neutron scatterer, still with sufficiently low stiffness and it should have a highly symmetric shape, like the VAMAS sample, cylindrical. If the sample is to comply with the plane stress condition, then to have a 2D shrink ring-and-plug system made of copper (or steel), a few mm in thickness and 30-40 mm in diameter would be a good candidate. Such systems are available in mass-production and they are bi-metallic coins. They are produced in almost all countries around the world from similar materials in similar size, though technologies of their production are expected to be different and undisclosed.

The aim of this study is to investigate residual stress in bi-metallic coins, using several easily obtainable candidates, and to assess how reasonably they can be used as standard specimens. The issues to investigate are

- How strong are the residual stresses in the coins? It is difficult to measure weak stresses since very small strain/stress error bars should be experimentally achieved.
- Is the material very anisotropic and should a special  $d_0$  be a part of the measuring programme?
- How uniform is the material? Since stamping of the surface image (relief) is not uniform, it can potentially induce non-uniformity in the stress state that should be avoided.
- Although there are expectations of tight standards and tolerances in the mint industry, can the consistency of minting technology and variability in the residual stress state (through years of minting and within the same year) be addressed and satisfactorily resolved in an experimental manner?

This is a first of the kind study on bi-metallic coin residual stress since no experimental results are available up to now. Beyond the particular consideration of bi-metallic coins as a stress standard, this work brings a new characterisation of these every-day objects.

### Principles of bi-metal coin production (minting)

The production process starts with punching coin blanks to be the ring and core/plug. A hole is also punched through a blank to produce a ring, whose diameter is accurately sized to fit inside the ring. The blank of the plug is also treated specially by adding a groove all the way around the edge e.g. by milling. The stamping (or double stamping) finally fixes the two parts of the assembly together and the force of the stamping plunger is adjusted to provide conditions for material of the inside edge of the ring to be pressed into the groove, locking the two parts into place (Fig. 1).

The different materials with different elastic and plastic properties, different sizes of ring and plug, different groove designs and tolerances are

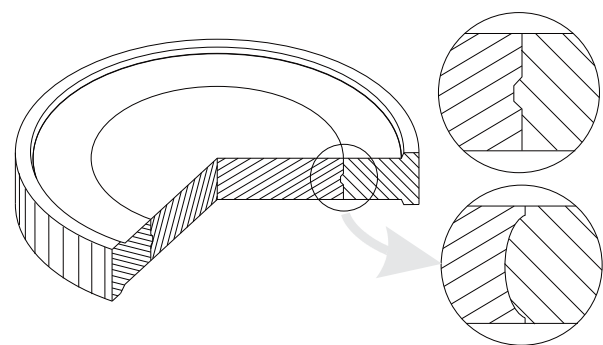


Fig. 1. Structure of a generic bi-metallic coin. A variable groove design is shown in two options.

reflected in different accumulated stresses. Although the locking mechanism by groove is partially responsible for the integrity of a bi-metallic coin, the residual stress should be generally present and also play a role.

**Samples and materials**

A number of bi-metallic coins were selected for the current study of the residual stresses and their details are given in Table 1. All selected coins are made from copper alloy of a certain kind (with few exceptions for the ring material) and all fall into a very narrow interval of sizes: 26 – 28 mm diameter.

**Experimental: principles**

Due to the plane stress condition the stress state of a bi-metallic coin with outer radius *b* and inner

Table 1. Bi-metallic coins and their characteristics (data collected from multiple sources)	
Coin	Description
	<b>UK2:</b> 2 pound coin (UK) Mass = 12 g; Diameter = 28.4 mm; Thickness = 2.5 mm Outer ring: Nickel-brass (76% Cu, 20% Zn and 4% Ni) Centre: Cupro-nickel (75% Cu, 25% Ni) Years of minting: 1997-present
	<b>CAN2:</b> 2 dollar coin, “toonie” (Canada) Mass = 7.30 g; Diameter = 28 mm; Thickness = 1.75 mm Outer ring: 99% Ni Inner core: aluminium bronze (92% Cu, 6% Al, 2% Ni) Years of minting: 1996–present
	<b>SA5:</b> 5 Rand coin (South Africa) Mass = 9 g; Diameter = 26 mm; Thickness = 2.8 mm Outer ring : Copper-Nickel Inner core: brass Years of minting: 2004–present
	<b>TW20:</b> 20 Yuan coin (Taiwan) Mass = 8.5 g; Diameter = 26.85 mm; Thickness = 2.15 mm Outer ring: Aluminium-bronze Inner core: copper-nickel Years of minting: 2001–present
	<b>MEX10:</b> 10 Pesos coin (Mexico) Mass = 10.329 g; Diameter = 28 mm; Thickness = 2.3 mm Outer ring Aluminium-bronze Inner core: Copper-nickel-zinc (65% Cu, 10% Ni, 25% Zn) Years of minting: 1997–present
	<b>Rus10:</b> 10 Rouble coin (Russia) Mass = 8.4 g; Diameter = 27 mm; Thickness = 2.1 mm Outer ring: Brass Inner core: Copper-nickel Years of minting: 1992–present
	<b>AUS5:</b> 5 dollar coin (Australia) Mass = 10.6 g; Diameter = 28.12 mm; Thickness = 2.6 mm Outer ring: Austenitic stainless steel Inner core : Aluminium bronze Years of minting: 1988–Present

radius  $a$  is extremely simple

$$\sigma_r^{ring}(r) = \frac{1}{(K^2 - 1)} \left( 1 - \frac{b^2}{r^2} \right), \quad \sigma_h^{ring}(r) = \frac{1}{(K^2 - 1)} \left( 1 + \frac{b^2}{r^2} \right), \quad \sigma_a^{ring}(r) = 0; \quad (1)$$

$$\sigma_r^{plug}(r) = -p, \quad \sigma_h^{plug}(r) = -p, \quad \sigma_a^{plug}(r) = 0; \quad (2)$$

where  $K = b/a$  and apart from the geometric dimensions is characterized by only one parameter  $p$ , a pressure on the plug. Stress-strain relationships are also simplified to

$$\sigma_h(r) = \frac{E}{(1 - \nu^2)(1 - 2\nu)} (\varepsilon_h + \nu\varepsilon_r);$$

$$\sigma_r(r) = \frac{E}{(1 - \nu^2)(1 - 2\nu)} (\varepsilon_r + \nu\varepsilon_h);$$

$$\varepsilon_a = \frac{\nu}{(1 - \nu)} (\varepsilon_h + \varepsilon_r).$$

(3)

In principle, for full reconstruction of the stress state, the stress measurement of the inner core is sufficient. Experimentally, the measurement programme might vary depending on assumption regarding  $d_0$  anisotropy:

(EXP1) If a  $d_0$  isotropy assumption is made, the experiment can be carried out non-destructively. The measurements of the central core involve detection of the two principal directions, hoop/radial and axial, from which by applying the condition of the axial component to be zero, the hoop/radial stress component and  $d_0$  can be resolved.

(EXP2) If, however,  $d_0$  is assumed to be anisotropic, the stresses can be resolved only in a destructive way. The experimental programme of the central core then involves detection of the two principal directions, hoop/radial and axial, each measured in loaded (intact coin) and unloaded (the central core is removed from the ring). Thus two principal elastic strains can be derived from the pair of measurement and the hoop/radial stress component can be calculated.

In both cases, due to the uniform stress state in the plug (Eq. 1, no radial dependence, only uniform pressure  $p$ ), measurements with an elongated gauge volume can be used reducing overall measurement time in this way and/or improving counting statistics. With the thickness range of the coins of 1.75 to 2.6 mm, and core diameters at least 15mm, a gauge volume with dimensions  $1 \times 1 \times 10 \text{ mm}^3$  seems the most adequate. Thus, measurements of the two directions (in transmission and reflection geometry) are easily possible, even for moderate performance neutron stress scanners.

### Experimental: neutron diffraction setup

Neutron residual stress measurements of bi-metallic coins were performed on the KOWARI neutron diffractometer at OPAL research reactor at ANSTO [2]. For all coins the Cu(311) reflection was used at 90°-geometry employing a neutron wavelength of  $\lambda = 1.54 \text{ \AA}$ . Because different alloys had slightly different lattice spacings, there was a natural variation in the exact position of the diffraction peak, but all of them they were within range of  $\pm 1^\circ$ .

A gauge volume with size of  $1 \times 1 \times 10 \text{ mm}^3$  was consistently used since it could be positioned within each and every coin central core. Not just one, but 5 locations (exact centre,  $\pm 3 \text{ mm}$ ,  $\pm 6 \text{ mm}$ ) were systematically measured for each coin to assess uniformity and statistical variations of the material of the plug with measurement times of 3 minutes. The high flux of KOWARI, optimised for this wavelength, yielded 50 - 60  $\mu\text{strain}$  accuracy on average or  $\sim 7\text{-}8 \text{ MPa}$  in terms of calculated stresses.

### Experimental: results and data analysis

The study has been performed in several steps:

First, the attempt was made to conduct a non-destructive experiment (EXP1), i.e. the inner core part was measured in two directions, hoop/radial and axial, to assess elastic strain anisotropy. The experimental results are presented in Fig. 2. As can be seen from the diagram, three out of seven coins demonstrate tension of the core. As this is a non-physical result, but rather an artefact of the data treatment, the assumption of isotropic  $d_0$  is not viable for the majority (if not all) of the coins.

Secondly, a full, but destructive analysis (EXP2) was performed next. The two principal directions, hoop/radial and axial, were measured in two states, intact and free, where the central core is removed from the ring. Stresses were calculated with properly measured  $d_0$  and are shown in Fig. 3. They are quite different from those shown in Fig. 2: with  $d_0$  taken correctly into account, all stresses are compressive, as expected.

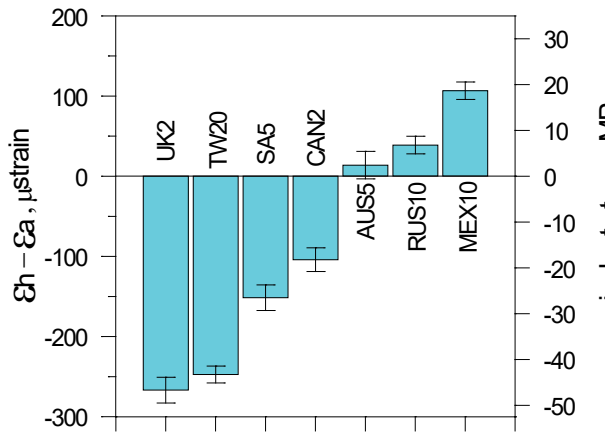


Fig. 2. Measure of the appeared anisotropy in strain and stress scale for seven bi-metal coins.

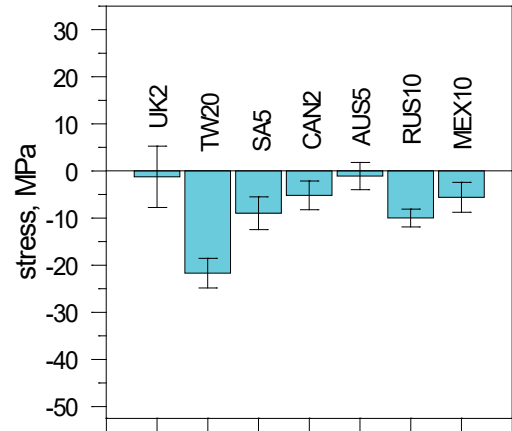


Fig. 3. Residual stress (negative pressure) for seven bi-metal coins.

Due to the significant anisotropy in coin UK2, additional measurements were made on it to assess in-plane anisotropy, uniformity and reproducibility. The dependence of the lattice d-spacing on the in-plane direction is shown in Fig. 4 (left) and indicates no in-plane anisotropy and non-uniformity, thus the cylindrical symmetry of coin is confirmed for this specimen. In comparison, the aluminium alloy AA7050 exhibits much larger degree of in-plane  $d_0$  anisotropy presented in Fig. 4 (right) inherited from the plate rolling process. To address the question of reproducibility, two UK2 coins were compared in intact conditions, from minting years 2002 and 2008, and within error bars they provided the same result. However, this coin is not the best sample to be used to check reproducibility of stress since the magnitude of stress turned out to be close to zero.

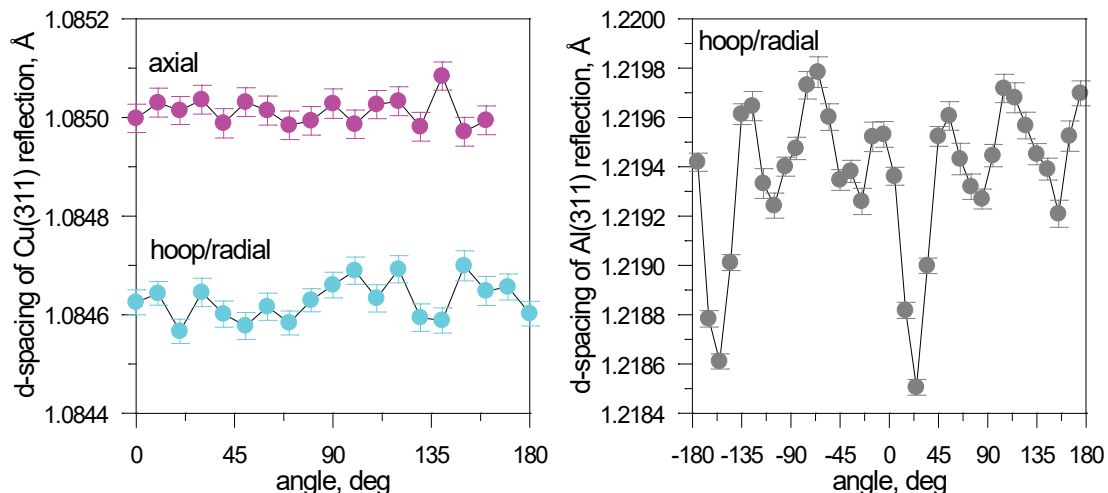


Fig. 4. In-plane isotropy of coin UK2 (left) in comparison with anisotropic angular dependence of AA7050 aluminium alloy used in the VAMAS sample (right).

## Discussion

A big discrepancy between Fig. 2 and 3 clearly shows that the anisotropy in  $d_0$  must be taken into account to obtain correct stress values and obtain physically meaningful results. Only then stress calculations result in the compressive state of the central core.

The selected set of seven coins revealed a significant variability of stresses ranging from near to zero stress in UK2 and AUS5 coins, to very low stress of  $\sim 5$ -10 MPa for coins CAN2, MEX10, SA5 and RUS10, to the highest stress of  $-22 \pm 4$  MPa for TW20 coin. Based on the results collected from this coin selection, coin TW20 can be considered the best candidate providing high stresses that can be easily measured. Considering the bi-metallic system as a whole, the stresses in the ring reach even higher values which can be demonstrated within the elastic model expressed in equations (1)-(2). The results of these calculations are given in Fig. 5.

The following considerations may suggest using the TW20 coin as a local/alternative standard:

- Stress measurements in the plug can be done extremely fast with an elongated gauge volume, e.g.  $1 \times 1 \times 10 \text{ mm}^3$ , achieving a good accuracy of 5-7 MPa. Only two directions are required to be measured and anisotropy of  $d_0$  is reduced to only two values. This cylindrical symmetry is more advantageous than the angular dependence of  $d_0$  for the VAMAS sample.

- More advanced and complete measurements can be also considered as a part of the measurement programme with measurements of the ring requiring longer measurement times while using  $1 \times 1 \times 10 \text{ mm}^3$  gauge volume. However, with stresses  $\sim 150$  MPa, the accuracy of stress determination can be reduced to 10-15 MPa which is still within easily achievable measurement times.

- On KOWARI, the total measurement time of one coin, both central coin and outer ring, takes (approximately) one day versus one week of beamtime to measure the VAMAS sample.

Overall, the material of coin TW20 (copper), its dimensions ( $\text{Ø}27$  mm and thickness 2.1 mm), the magnitude of stress, the uniformity and in-plane isotropy of the material, makes it the best candidate for being an alternative “ring-and-plug” standard suitable for fast neutron measurements.

## Summary

Several bi-metallic coins were studied using neutron diffraction and their residual stress state was determined. For the coins the stress varied between a few MPa to -22 MPa in the TW20 coin.

Due to the nature of the material and its thermo-mechanical treatment during processing, the  $d_0$  anisotropy consistently occurs for all coins. Therefore, a ring and plug measurement, in the disassembled condition is required for a proper  $d_0$  measurements and an overall stress analysis.

Although questions of anisotropy and uniformity and reproducibility were addressed, at least for coins of the UK2 types, a more systematic research is still required, namely for coins TW20, which so far are considered the best candidate for an alternative standard sample for fast and easy stress calibrations.

## References

- [1] Webster, G. A., 2000, Neutron diffraction measurements of residual stress in a shrink-fit ring and plug VAMAS Report no. 38: National Physical Laboratory.
- [2] Kirstein, O., Luzin, V., and Garbe, U., 2009, The Strain-Scanning Diffractometer Kowari: Neutron News, v. 20, no. 4, p. 34-36.  
<http://dx.doi.org/10.1080/10448630903241175>

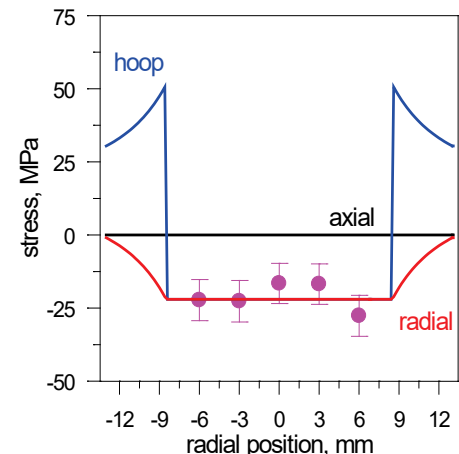


Fig. 5. Stress distribution (experimental and calculated) in coin TW20.

# Residual Stress Measurements Inside a Small Inner Diameter Hole at Low Bragg Angle Using X-Ray Diffraction Technique

M. Belassel<sup>1,a\*</sup>, J. Pineault<sup>1,b</sup>, M. Brauss<sup>2,c</sup>.

<sup>1</sup>Proto Manufacturing Limited, 2175 Solar Crescent, Oldcastle, Ontario, Canada

<sup>2</sup>Proto Manufacturing Inc., 12350 Universal Drive, Taylor, Michigan, 48180, USA

<sup>a</sup>mbelassel@protoxrd.com, <sup>b</sup>xrdlab@protoxrd.com, <sup>c</sup>mbrauss@protoxrd.com

**Keywords:** Residual Stress, Bolt-Hole, Inner Diameter, Low Bragg Angle, Abusive Machining

**Abstract.** A new X-Ray diffraction (XRD) goniometer has been specially developed to nondestructively measure residual stress (RS) on the inner diameter (ID) of small holes in metal and ceramic components. The major advantage of this novel goniometer is its ability to perform RS measurements on the ID of small holes without the need to section the component, thus maintaining the integrity of the residual stress field inherent to the component of interest. This new patented XRD goniometer has been used on a wide variety of aerospace components on features such as holes in airframe/structural components, as well as fastener/bolt holes, air holes, and confined areas on rotating and non-rotating turbine engine components. In many instances, measurements can be performed at  $2\theta$  angles much lower than the widely accepted lower limit of approximately  $130^\circ$ . The selection of the actual Bragg angle used depends upon the material itself, the hole ID, and the thickness of the component. Results obtained indicate that the new goniometer can be used to measure RS on the ID of small holes with good accuracy and precision even at relatively low  $2\theta$  angles in the vicinity of  $100^\circ$ .

## Introduction

Since the discovery of RS and its measurement early in the last century, measurement techniques have been evolving steadily [1]. Many techniques have been developed thanks to industry demand and specific needs [2]. Many RS measurement techniques exist and each generally requires a different experimental setup; laboratory equipment is often suitable for small parts, whereas portable systems are generally required for oversized parts. Moreover, the geometry of the XRD goniometer may vary to facilitate access to the measurement locations of interest on a component. Both Psi and Omega modes have been widely implemented on most current XRD RS measurement instruments. Omega mode is suitable for tight geometries such as grooves as may be found in the root of a gear tooth when measuring along the groove (i.e. parallel to the teeth), whereas Psi mode in turn is more adapted to measurements in the direction normal (perpendicular) to the groove (such as the opening of the groove permits). Each geometry has its advantages and disadvantages and each may be complementary in certain instances.

In this study, RS analysis will be extended to measurements on the ID of bolt holes in the hoop direction. Such measurements are applicable for both automotive and aerospace materials; this study includes examples on a Ni-Base super-alloy. For these applications, a new XRD instrument and goniometer were designed and fabricated that operate in Psi mode [3].

### Stress Measurement Technique

**Basic Principles.** The x-ray diffraction technique uses the distance between crystallographic planes, i.e. the d-spacing, as a strain gage in a crystalline material. When the material is in tension, the d-spacing increases and when the material is in compression, the d-spacing decreases. The presence of residual stresses in a material produces a shift in the x-ray diffraction peak angular position that is directly measured by the detector [3]. The diffraction angle  $2\theta$  is measured experimentally and the d-spacing is then calculated using Bragg's law:

$$n\lambda = 2d \sin \theta \quad (1)$$

Where:  $\lambda$  is the wavelength of the radiation.

Diffraction peaks collected should have a sufficient peak/background ratio and a limited noise level. These will depend on the  $\{hkl\}$  plane selected, the collection time, the size of the irradiated area and the material microstructure. Once the d-spacing is measured for unstressed  $d_0$  and stressed  $d$  conditions, the strain is calculated using either of the following relationships:

$$\varepsilon = \frac{(d - d_0)}{d_0} \quad \text{or} \quad \varepsilon = -\frac{1}{2} \cot(\theta) \cdot \Delta(2\theta) \quad (2)$$

To improve measurement accuracy when determining  $\Delta(2\theta)$ , the  $\theta$  angle selected should be close to  $90^\circ$  (i.e.  $2\theta \sim 180^\circ$ ). The widely published and agreed upon low limit for  $2\theta$  is  $130^\circ$ ; using  $2\theta$  values below this will diminish  $\Delta(2\theta)$  resolution and as such will result in a loss in RS measurement accuracy and a concomitant increase in experimental error. The plot in Figure 1 demonstrates the relationship between  $\Delta(2\theta)$  for various  $2\theta$  values. As  $2\theta$  decreases so does the slope, indicating a reduced resolution in peak separation.

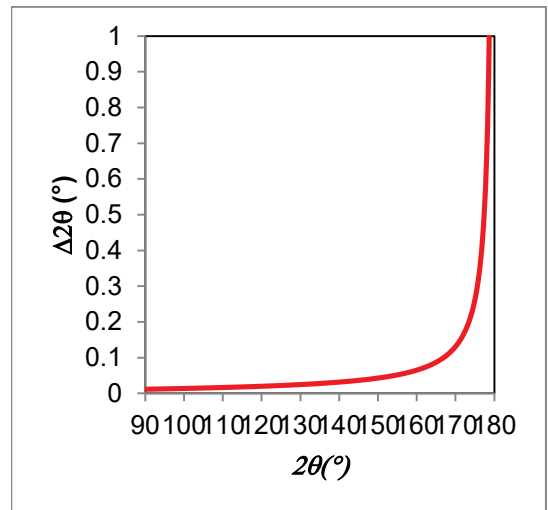


Figure 1: Variation in  $\Delta(2\theta)$  resolution with diffraction angle  $2\theta$ .

**Sin<sup>2</sup>ψ Method.** For the  $\sin^2\psi$  method, where a number of d-spacings are measured, stresses are calculated from an equation derived from Hooke's law for isotropic, homogeneous, fine grain materials,  $\psi$  is the angle subtended by the bisector of the incident and diffracted beam and the surface normal, and  $\phi$  is the direction of stress measurement [4].

$$\frac{d_{\phi\psi} - d_0}{d_0} = \frac{1}{2} S_2^{hkl} (\sigma_\phi - \sigma_{33}) \sin^2 \psi + \frac{1}{2} S_2^{hkl} \sigma_{33} - S_1^{hkl} (\sigma_{11} + \sigma_{22} + \sigma_{33}) + \frac{1}{2} S_2^{hkl} \tau_\phi \sin 2\psi \quad (3)$$

Where:  $\varepsilon_{\phi\psi}$  is the strain at a given  $\psi$ ,  $\phi$  tilts,  $\frac{1}{2} S_2^{hkl}$  and  $S_1^{hkl}$  are the x-ray elastic constants of the material.

**Materials and Measurement Conditions**

The material of interest for this study is a Ni-base super-alloy. Three examples of surface conditions that can be found on the ID of machined holes were investigated as follows:

1. Hole drilled with no coolant.
2. Hole drilled with coolant.
3. Drilled, honed and shot peened hole.

Residual stress versus depth profiles were collected on the face of each of the machined holes using conventional XRD instrumentation and on the ID of the same holes using a new XRD instrument. The measurement conditions were as follows: 1) for the conventional instrument operating in Omega mode, the {311} diffraction plane was selected for measurements at  $2\theta=151.9^\circ$  using  $Mn_{k\alpha}$  radiation ( $\lambda=2.1034$  Angstroms), and 2) for the new instrument operating in Psi mode, the {311} diffraction plane was selected for measurements at  $2\theta=111.3^\circ$  using  $Co_{k\alpha}$  radiation ( $\lambda=1.7902$  Angstroms). Selection of the diffraction angle  $2\theta$  to be employed using the new instrument is predicated upon the diameter of the hole ( $D$ ), and the thickness of the component ( $W$ ). A geometric relationship can thus be established as seen in Eq. 4 and in Figure 2:

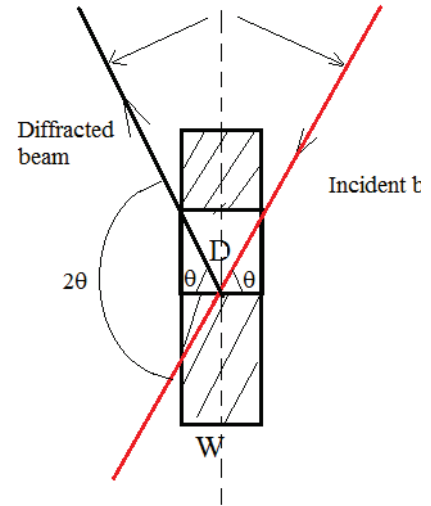


Figure 2: Determining optimal  $2\theta$  for use on the ID of a hole using new Psi mode instrument.

$$\tan(\theta_{\max}) = \frac{2D}{W} \tag{4}$$

For Ni-base super-alloys where the actual collimator and the detector size are taken into account, the optimal  $2\theta$  to use is  $111.3^\circ$ . In this case, the ratio is:  $\frac{2D}{W} = 4$ ,  $2\theta_{\max} = 152^\circ$ , which is widely sufficient for this experiment. For other materials, the ratio may vary according to the Bragg conditions available for use and the component geometry.

In Figure 3, the RS on a Ni-base super-alloy turbine engine disk is being measured using: a) a conventional Omega mode instrument on the face of the hole, and b) using the new instrument in Psi mode on the ID of the same hole.

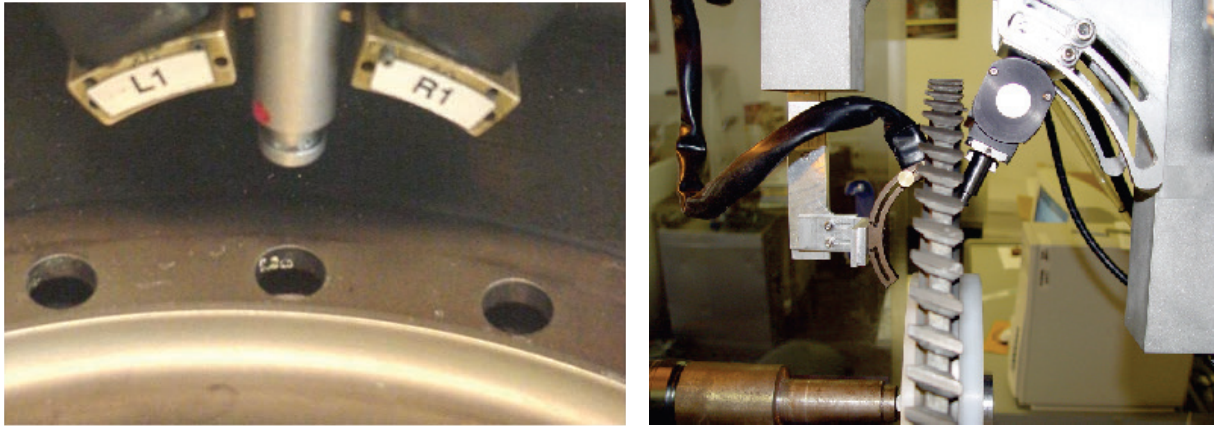


Figure 3: Measuring RS a) on the face of machined holes using a conventional XRD instrument and b) on the ID of machined holes using the new XRD instrument

### Results and Discussion

Prior to performing RS measurements, the alignment of the instrument was verified using a stress free Ni powder as per ASTM E915 [5], as well as a known high stress proficiency standard.

Microstructure characterization of the different processes revealed the following:

1. The hole drilled with no coolant exhibited severely distorted grains and undesirable microstructure near the hole ID surface.
2. The hole drilled with coolant exhibited only slightly distorted grains near the hole ID surface.
3. The drilled, honed and shot peened hole showed no signs of abusively machined material.

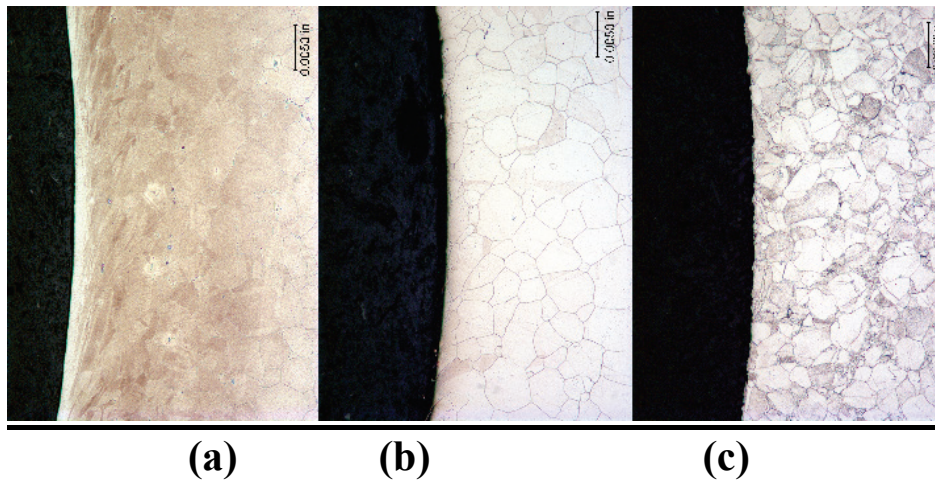


Figure 4 – Hole cross sections (ID to the left) of holes machined as follows: a) drilled with no coolant, b) drilled with coolant, and c) drilled, honed and shot peened.

The RS vs. depth results obtained on both the face of the hole, and the ID of the hole, can be seen in Figure 5. The results obtained on the ID of the machined holes were found to be much more effective for detecting the relatively thin tensile stressed layers inherent to the various machining and cold working processes applied. In the case of the hole drilled with coolant, RS that appeared compressive on the face of the disk, was found to be tensile on the hole ID. In the case of the hole drilled without coolant, the magnitude of the tensile RS found on the ID was much greater when compared to tensile RS found on the face of the disk. Thus, the very steep stress gradients produced by machining demand nondestructive measurement of RS on the ID.

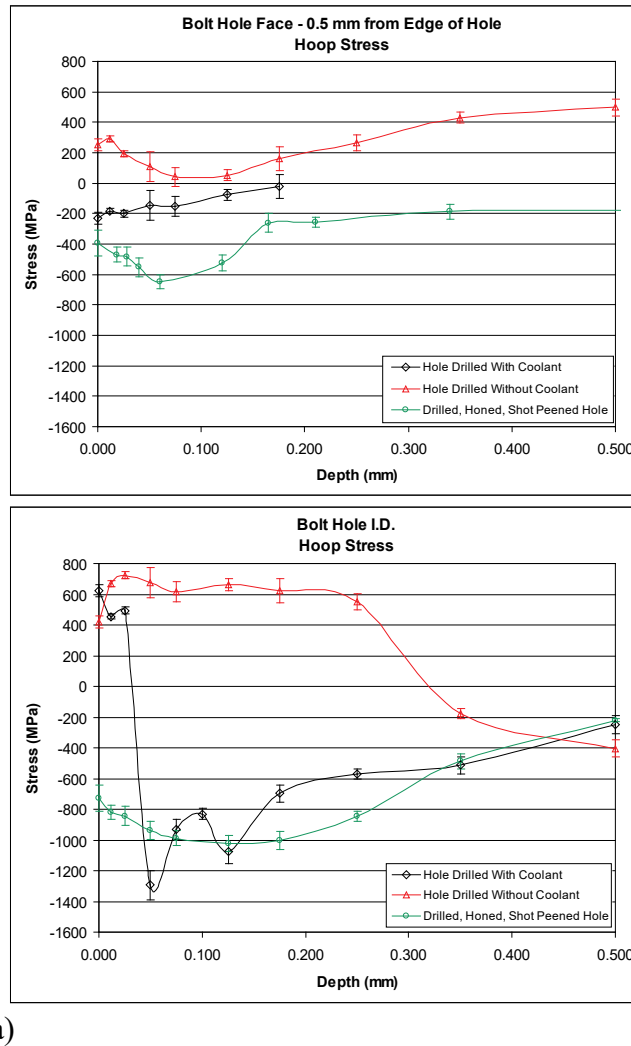


Figure 5: Stress vs. depth profiles a) on the face of machined holes using a conventional XRD instrument, and b) on the ID of machined holes using a new XRD instrument.

Clearly, the new XRD instrument adapted for measurements on the ID surface was more effective in revealing the actual stress gradients present i.e., it was more effective in revealing the effect of each machining and cold working processes applied as well as the associated depth, sign and magnitude of undesirable tensile RS [6]. This ability is critical for the aerospace industry where accurate RS measurements are needed to help improve and optimize the machining and cold working processes applied to life limiting components so as to insure a long service life of such components.

The experimental errors associated with the  $2\theta$  angles selected should be higher for low  $2\theta$  and vice versa [1]. The magnitude of the experimental errors obtained in this study was deemed good given the magnitude of the RS present and the associated RS gradients observed [7]. The magnitude of the experimental errors were found to be dependent upon the RS levels measured, as well as the material condition and microstructural effects present in the hole that were investigated. A detailed methodology to successfully measure RS at a suitable Bragg angle ( $2\theta$ ) was developed prior to applying it to real components. This methodology also employs a statistical approach where each measurement is reproduced to guarantee its accuracy.

### Summary

New goniometer head geometry has been developed and successfully applied to a new instrument that can be used to measure RS on the ID of small holes nondestructively. Such measurements were heretofore impossible to execute without sectioning the component. The application of this technique on real components presented many challenges that were addressed using a new, high accuracy instrument (and associated methodology) to reliably measure RS on the ID of small holes. Moreover, the new instrument provided RS results that correctly characterized the actual RS state present on the disk hole ID where a conventional instrument failed. This new instrument thus opens the way to the accurate evaluation of RS on the ID of small holes which is of great interest to both industry in general, and to the aerospace industry in particular.

### References

- [1] V. Hauk, “Structural and Residual Stress Analysis by Nondestructive Methods”, Elsevier, Amsterdam, 1997.
- [2] J.A. Pineault, M. Belassel, M.E. Brauss, “X-Ray Diffraction Residual Stress Measurement in Failure Analysis”, Failure Analysis and Prevention, Vol. 11, ASM Metals Handbook, American Society for Metals, 2002, p. 484-497.
- [3] M.Brauss, Proto Patent No. US 7,283,612 B2, issued October 16, 2007 for X-Ray Diffraction Method.
- [4] Noyan I.C. and Cohen J.B., ‘Residual Stress’, Springer Verlag, 1987.  
<http://dx.doi.org/10.1007/978-1-4613-9570-6>
- [5] ASTM E915-10, “Standard test method for verifying the alignment of x-ray diffraction instrumentation for residual stress measurement”.
- [6] M. Belassel et al., “Effect of Thermal and Mechanical Loading on the Generation of Macro and Micro Stresses in Eutectoid Steel”, Proc. 4th Int. Conf. Residual Stresses, ICRS 4. Soc. Exp. Mechanics, 1994, 392-401.
- [7] J. Lu et al. “Handbook of Measurement of Residual Stresses”, SEM, Published by the Fairmont Press, Inc., 1996.

# Comparison of Residual Stress Measurement Techniques and Implementation Using X-Ray Diffraction

M. Belassel<sup>1,a\*</sup>, J. Pineault<sup>1,b</sup>, N. Caratanasov<sup>1</sup>, M. Brauss<sup>2,c</sup>

<sup>1</sup>Proto Manufacturing Limited, 2175 Solar Crescent, Oldcastle, Ontario, Canada

<sup>2</sup>Proto Manufacturing Inc., 12350 Universal Drive, Taylor, Michigan, 48180, USA

<sup>a</sup>mbelassel@protoxrd.com, <sup>b</sup>xrdlab@protoxrd.com, <sup>c</sup>mbrauss@protoxrd.com

**Keywords:** Residual Stress, X-Ray Diffraction, Measurement Technique, Geometry

**Abstract.** Regardless of the particular residual stress (RS) measurement technique being used, all are based on the same basic principles when using x-ray diffraction (XRD). Every technique has both its advantages and disadvantages, many of which are well known to engineers and scientists however, some of the important “finer points” are unfortunately not widely discussed or known by those not well versed in the subject. This paper will try to bring to light many of these commonly misunderstood issues by comparing the different techniques and attempt to illuminate the associated problems a user may encounter when measurements become challenging i.e. when RS measurements are to be performed in tight grooves or on textured materials for example. In this study, different techniques including the:  $\text{Cos}\alpha$  technique, MET (used in Psi, Omega, or Modified Psi mode) have been evaluated and tested on a variety of materials and geometries.

## Introduction

RS measurements using XRD techniques were first performed as early as 1925 [1]. Since then, measurement techniques and equipment slowly evolved in the following decades and major improvements were realized in the 1970s and the 1980s. Many RS measurement techniques based on XRD have been developed and implemented on a variety of instruments that are widely used in industry and academia today. As the use of XRD became more widespread in the 1950s, a technique called the Single Exposure Technique (SET) was commonly used however, it had very limited accuracy and did not work well on materials that did not possess a near random grain orientation distribution. Furthermore, the SET used only 1 data point, and relied on precise knowledge of the unstressed lattice spacing which was often difficult to determine experimentally with sufficient accuracy on the actual components or samples under investigation. As such, the quality of the data was very difficult to assess because non-linear relationships cannot be observed with only 2 data points. Due to the inherent limitations of the SET, scientists and engineers developed a new technique called the Multiple Exposure Technique (MET) which uses many more data points resulting in high confidence RS measurement results that do not rely on knowing the unstressed lattice spacing a priori [2]. Since then, many related standards have been developed, accepted and applied to the measurement of RS via XRD worldwide.

In this study, different techniques including the:  $\text{Cos}\alpha$  technique, MET (used in Psi, Omega, or Modified Psi mode) will be evaluated and tested on a variety of materials and geometries. This paper will emphasize the different findings and the limitations associated with each of the techniques evaluated.

## Principles

**Generalized technique:** these principles apply to MET when used in either Omega or Psi mode. The XRD technique uses the distance between crystallographic planes, i.e. d-spacing, as a strain gage and can only be applied to crystalline, polycrystalline and semi-crystalline materials [2]. When the material is in tension, the d-spacing increases and when the material is in compression, the d-spacing

decreases. The presence of RS in the material produces a shift in the XRD peak angular position that is directly measured by the detector [3]. For a known x-ray wavelength  $\lambda$  and  $n$  equal to unity, the diffraction angle  $2\theta$  is measured experimentally and the d-spacing is then calculated using Bragg's law:

$$n\lambda = 2d \sin \theta \tag{1}$$

Where  $\lambda$  is the wavelength of the radiation. Once the d-spacing is measured for unstressed ( $d_0$ ) and stressed ( $d$ ) conditions, the strain is calculated using the following relationship:

$$\varepsilon = (d - d_0)/d_0 \tag{2}$$

For the  $\sin^2\psi$  method where a number of d-spacings are measured, stresses are calculated from an equation derived from Hooke's law for isotropic, homogeneous, fine grain materials:

$$\varepsilon_{\phi\psi} = \frac{1}{2} S_2 (\sigma_{\phi} - \sigma_{33}) \sin^2 \psi + \frac{1}{2} S_2 \sigma_{33} - S_1 (\sigma_{11} + \sigma_{22} + \sigma_{33}) + \frac{1}{2} S_2 \tau_{\phi} \sin 2\psi \tag{3}$$

Where,  $\frac{1}{2} S_2$  and  $S_1$  are the x-ray elastic constants of the material,  $\sigma_{\phi}$  is the stress in the direction of the measurement  $\phi$ ,  $\psi$  is the angle subtended by the bisector of the incident and diffracted x-ray beam and the surface normal, and  $\varepsilon_{\phi\psi}$  is the crystallographic strain at a given  $\psi$  tilt, see figure 1.

The main difference between the Omega and Psi modes can be seen in the defocusing effects observed at high  $\psi$  angles. RS measurements performed in Psi mode are relatively insensitive to defocusing errors when compared to Omega mode. The increased defocusing effect and associated errors observed in Omega geometry can be mitigated by employing two detectors which can be used to minimize the magnitude of negative  $\psi$  angles employed in a RS measurement and thus minimize defocusing errors. At the same time, care must be taken in the selection of the incident x-ray beam size to limit both defocusing and beam divergence errors [2]. Moreover, Psi mode offers a constant absorption of x-rays for all  $\psi$  tilts due to the constant x-ray path whereas, in Omega mode the absorption varies with the  $\psi$  tilt angle and requires a correction. The depth of penetration is very similar for both modes except at high  $\psi$  tilt angles [4].

**Modified Psi.** When working in Modified Psi mode which is a special geometry set-up convenient for vertical beam direction, the x-ray

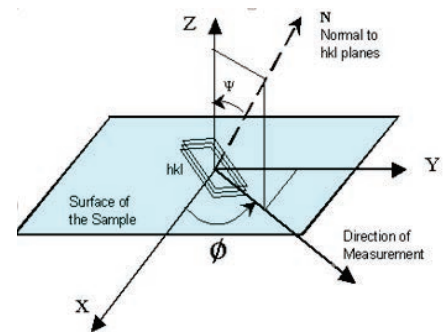


Figure 1: Definition of the axis and the direction of measurement.

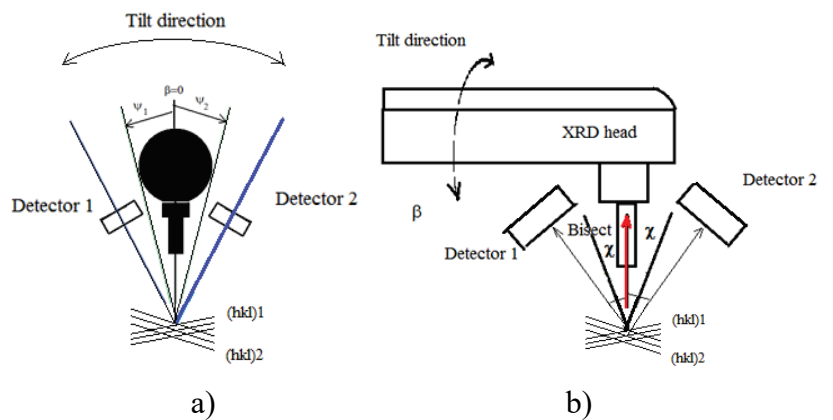


Figure 2: Goniometer geometries: a) Omega mode and b) Modified Psi mode.

beam is perpendicular to the surface of the sample and the diffracting {hkl} planes lie in a plane with an angular offset of  $(180-2\theta)/2$  and the  $\psi$  angles for each plane vary with the inclination, see figure 2. In this case, for each normal to the {hkl} plane, the  $\phi$  and  $\psi$  are a function of the goniometer tilt angle as shown in Eq. 4. The relationship between the  $\beta$ ,  $\chi$ ,  $\psi$ , and  $\phi$  angles are shown in Eq. 4 and Eq. 5.

$$\cos \psi = \cos \beta \cdot \cos \chi \tag{4}$$

$$\cos \phi = \frac{\sin \beta \cdot \cos \chi}{\sin \psi} \tag{5}$$

Where  $\beta$  is the tilt angle and  $\chi$  is the offset angle between the incident beam and the bisector of incident and diffracted beams. The derived Eq. 6 is shown as follows:

$$\begin{aligned} \varepsilon = & \frac{1}{2} S_2 (\sigma_{11} \sin^2 \beta \cos^2 \chi + \sigma_{22} \sin^2 \chi) \\ & + \frac{1}{2} S_2 (\tau_{12} \sin \beta \sin 2\chi + \tau_{13} \sin 2\beta \cos^2 \chi + \tau_{23} \cos \beta \sin 2\chi) + C \end{aligned} \tag{6}$$

The technique does not provide a direct measurement of the shear stress which is necessary when dealing with curved surfaces and non uniform processes applied to heterogenous materials. This technique also requires two detectors at opposite  $\phi$  angles [5]. The most accurate measurement for this configuration is a triaxial measurement where tilt angles  $\psi$ ,  $\phi$  can be correctly used as in the  $\text{Sin}^2\psi$  method [6].

**Cos( $\alpha$ ) method.** This method uses the diffraction ring (also called the Debye Ring) where the position of the peak at each angle  $\alpha$  around the ring is measured [7]. This special set-up which doesn't required any change in the incident angle. Using the relationship between the derived strains in Eq. 7 and Eq. 8, one can plot the strain as a function of  $\cos \alpha$  to calculate the normal stress  $\sigma_{11}$  and as a function of  $\sin \alpha$  to calculate the shear stress  $\sigma_{12}$ .

The constitutive equations are as follows:

$$\varepsilon_{\alpha 1} = \frac{1}{2} [(\varepsilon_{\alpha} - \varepsilon_{\pi+\alpha}) + (\varepsilon_{-\alpha} - \varepsilon_{\pi-\alpha})] = \frac{1}{2} S_2 \cdot \sigma_{11} [\sin^2(\psi_0 - \eta) - \sin^2(\psi_0 + \eta)] \cos \alpha \tag{7}$$

$$\varepsilon_{\alpha 2} = \frac{1}{2} [(\varepsilon_{\alpha} - \varepsilon_{\pi+\alpha}) - (\varepsilon_{-\alpha} - \varepsilon_{\pi-\alpha})] = \frac{1}{2} S_2 \cdot 2\tau_{12} \cdot (\sin 2\eta \sin \psi_0) \sin \alpha \tag{8}$$

Where  $\psi_0$  is the inclination of the sample relative to the goniometer,  $2\eta$  is the angle subtended by the incident beam and diffracted beam, and  $\varepsilon_{\alpha}$ ,  $\varepsilon_{\pi+\alpha}$ ,  $\varepsilon_{-\alpha}$  and  $\varepsilon_{\pi-\alpha}$  are the measured strains from sectors of the ring as shown on figure 3.

When using Eq. 7 and Eq. 8, it is necessary that symmetrically opposite peaks are available on the Debye Ring. It should be noted that  $\psi_0 \neq 0^\circ$  when using this technique. It is recommended to tilt the head in such a way that one side of the Debye Ring represents  $\psi$  angles close to  $0^\circ$ , and the other side of the ring

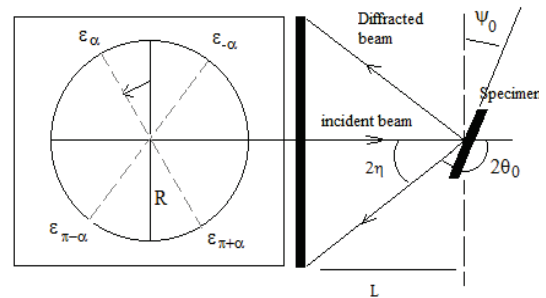


Figure 3: Principle of Cos  $\alpha$  method using Debye Ring

represents  $\psi$  angles as high as possible to better represent the strains present. The shear stress  $\sigma_{12}$  provided by this technique is not of interest at this moment.

### Experiments

Three samples were selected for RS measurement on the surface employing all of the aforementioned techniques. The samples were as follows: 1) a shot peened flat steel sample with a grooves that were flat at the bottom with nominal stress of  $-450 \pm 35$  MPa, 2) an aluminum plate with low stress that exhibits some preferred orientation, and 3) a flat shot peened Ni-base alloy sample with a nominal stress of  $-1040 \pm 50$  MPa. No measurements were performed with Psi and Modified Psi modes on this sample. The error reported is only 1 Standard deviation.

In the case of the steel sample, RS measurements were collected in both the axial direction parallel to the grooves, and in the direction transverse to the grooves. The groove dimensions were as follows: Groove 1 (GR1): 2 mm wide by 1.5 mm deep, and Groove 2 (GR2): 2 mm wide by 2 mm deep. The most important parameters that determine the capability of any measurement technique and associated goniometer hardware to successfully measure RS in confined areas such as grooves are: 1) the angular opening between the incident beam and diffracted beam, and 2) the direction of  $\psi$  tilting associated with the RS measurement. RS measurements were performed employing 4 different goniometers thus using all available geometries.

All of the RS measurements on the steel and aluminum samples were performed using Cr  $\alpha$  ( $\lambda=2.291\text{\AA}$ ) x-radiation diffracting from the {211} plane at  $156^\circ 2\theta$ , and the {222} plane at  $157^\circ 2\theta$  respectively. RS measurements on the Ni-base alloy sample were performed using Cr  $\beta$  ( $\lambda=2.08487\text{\AA}$ ) x-radiation diffracting from the {311} plane at  $149^\circ 2\theta$  when using the  $\text{Cos}(\alpha)$  technique, and Mn  $\alpha$  ( $\lambda=2.10314\text{\AA}$ ) x-radiation diffracting from the {311} plane at  $152^\circ 2\theta$  when using the other techniques. Table 1 lists the available angular tilt range  $\psi$  for each technique using the diffraction conditions reported above. The aperture size used in the experiment was 1 mm except the cos  $\alpha$  where the aperture was 2 mm. A mask is applied on the top around the grooves to avoid any diffraction from those surfaces.

Table 1: Goniometer capability and ranking for GR1:W:2 mm x D:1.5 mm, GR2:W:2 mm x D:2 mm

Goniometer Geometry/Mode	Technique	Angular opening ( $^\circ$ )	Angle GR1 @ $\psi=0$ ( $^\circ$ )	Angle GR2 @ $\psi=0$ ( $^\circ$ )	Selection (Groove)
PSI	$\text{Sin}^2\psi$	24	33.7	26.5	Transverse
Omega	$\text{Sin}^2\psi$	48	33.7	26.5	Axial
Modified PSI	$\text{Sin}^2\beta$	48	33.7	26.5	Transverse
Debye Ring	$\text{cos}\alpha$	48	33.7	26.5	None

As such, when measuring RS in the bottom of grooves it is desirable to have a goniometer (or 2 goniometers) that work in both Psi and Omega modes so as to enable RS measurements in two directions.

### Results and Discussions

RS measurements were performed employing the 4 different goniometers. The results reported in table 2 indicate that the RS measurements in the axial direction were performed relatively easily in GR1 using all of the techniques. RS measurements performed in the transverse direction in GR1 were possible using Psi and Modified Psi with reduced accuracy due to the limited  $\psi$  tilt range available. RS measurements in the transverse direction of GR1 were not possible using  $\text{Cos}\alpha$  and Omega because of the very limited  $\psi$  tilt range available in these geometries. Any result not within 2 standard deviation for each material is considered failed.

Table 2: RS measurement results on different head goniometer geometries and techniques.

Goniometer Geometry/Mode	Technique	Direction	Steel sample GR1 (-470±70 MPa)	Steel sample GR2 (-450±70 MPa)	Al sample Low stress <50MPa	Ni-Base alloy sample (-1040±100MPa)
PSI	$\text{Sin}^2\psi$	Axial	-524±19	-228±36*	+28±8	N/A
		Trans	-526±15*	-204±26 <sup>F</sup>	+1±10	
OMEGA	$\text{Sin}^2\psi$	Axial	-435±8	-475±5	+12±13	-1070±50
		Trans	F	F	-21±6	
Modified PSI	$\text{Sin}^2\beta$	Axial	-443±5	-596±11 <sup>F</sup>	+18±12	N/A
		Trans	-386±19*	-188±46 <sup>F</sup>	+13±8	
Debye Ring (2D detector)	$\text{Cos}\alpha$	Axial	-485±42	-642±234 <sup>F</sup>	-29±31	-719±50 <sup>F</sup>
		Trans	F	F	-86±10 <sup>F</sup>	

Note: \* indicates results were corrected after removing bad data points, F indicates a failed measurement  
 N/A indicates data not available

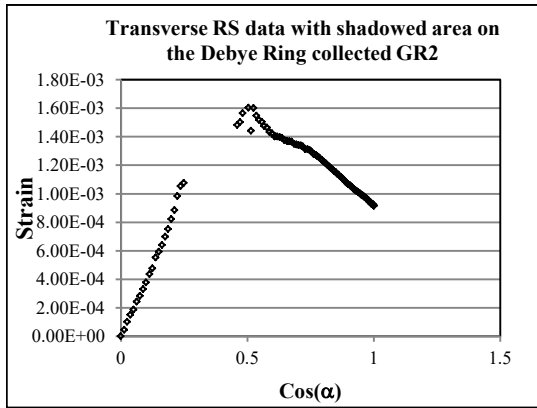


Figure 4: Strain vs.  $\text{Cos}\alpha$  data plot observed measuring RS in the groove area

angle. For  $\text{Cos}\alpha$ , because of the  $\psi$  tilt angular range necessary to perform a reliable RS measurement, a portion of the Debye-Ring is masked (or shadowed) and the data obtained is rendered unusable i.e., when using the  $\text{Cos}\alpha$  technique on GR2, high  $\psi$  angles are not an option so the data missing from the Debye-Ring renders the strain calculation useless (see Figures 4 and 5). As an analogy, this is equivalent to attempting to use Psi or Omega Modes to calculate the shear stress when all of the positive (or negative)  $\psi$  tilts are not available for the calculations.

One approach to making all the above techniques successful is to remove the material around the location of interest (i.e. the bottom of the groove) so as to expose the location of interest. The disadvantage to this approach is that the part must be sacrificed at the expense of the RS measurements and as such only non-production parts would be analyzed.

For GR2, the RS measurements failed in all directions in all Modes except using Omega Mode in the axial direction. Omega-Mode is the only one that is capable of accurately measuring RS in the bottom of a very narrow, deep groove in the axial direction. In such cases, the beam size must be selected carefully and in some instances, a mask on top of the groove may be used to obtain reliable RS results. The success of Psi-Mode in the axial direction is related to the narrow angle opening between the beam and the detector (i.e. the high back reflection  $\{hkl\}$  selected in this particular instance). The Psi-Mode data was corrected after removing bad points at high  $\psi$  tilt

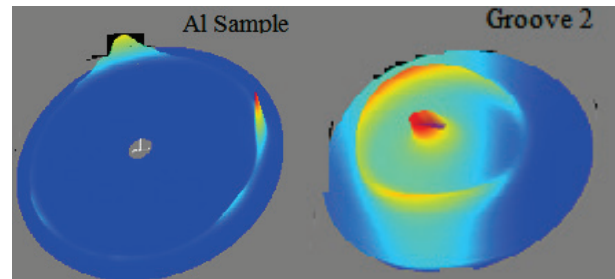


Figure 5: Debye Ring data measured in the groove 2 and Al sample

For the aluminum sample, all methods were capable of producing RS results within an acceptable range however, some scatter was observed due to the texture present in the material only, no size effect was observed during the measurements. The  $\text{Cos}\alpha$  technique had more difficulties and the measurements were repeated few times before a stress value could be calculated [8]. This is because of spotty data on the Debye Ring. This confirms the problem with the shadowing effect observed in the grooves. When looking at the slope of the data curve for a given RS value, the  $\text{Cos}\alpha$  technique has a reduced slope when compared to the other techniques [9]. This explains the high experimental errors in the RS values.

When perform RS measurements on the Ni-Base alloy sample, the  $\text{Cos}\alpha$  technique failed due to the weak peak intensity collected using  $\text{Cr}_k\beta$  line. RS measurements using the Omega technique worked well however no measurements were performed with Psi and Modified Psi modes on this sample .

### Summary

The results obtained indicate that amongst the various techniques applied to RS measurement, the MET using  $\text{Sin}^2\psi$  was capable of measuring RS on a wide variety of materials with different geometries and material conditions whereas the  $\text{Cos}\alpha$  technique was limited to isotropic materials and near flat surfaces. Moreover, the Omega-Mode was the only one that was capable of measuring RS in deep grooves in the axial direction. The use of Psi-Mode may be advantageous when tight constraints related to the geometry of the test specimen become an issue. The Psi-mode goniometer is preferred when compared to the Modified Psi-mode goniometer because the latter is more limited in terms of sample geometry constraints and the scattering vector is offset from the  $\psi$  tilt plane. For successful RS measurements on a wide variety of components as well as in confined spaces and complex geometries, a combination of Psi and Omega Modes are ideal. For the  $\text{Cos}\alpha$  technique to be viable for RS measurement, more development would be required to deal with scattered data on the Debye Ring and its various geometric limitations.

### References

- [1] LESTER, H. H., and ABORN, R. H. Behavior Under Stress of the Iron Crystals, Army Ordnance, v. 6, 1925, 1926, pp. 120, 200, 283, 364
- [2] Noyan I.C. and Cohen J.B., 'Residual Stress', Springer Verlag, 1987.  
<http://dx.doi.org/10.1007/978-1-4613-9570-6>
- [3] J.A. Pineault, M. Belassel, M.E. Brauss, "X-Ray Diffraction Residual Stress Measurement in Failure Analysis", Failure Analysis and Prevention, Vol. 11, ASM Metals Handbook, American Society for Metals, 2002, p. 484-497.
- [4] V. Hauk, "Structural and Residual Stress Analysis by Nondestructive Methods", Elsevier, Amsterdam, 1997.
- [5] EN 15305, "Non-destructive Testing - Test Method for Residual Stress analysis by X-ray Diffraction", August 2008.
- [6] J. Lu et al., "Handbook of Measurement of Residual Stresses", Published by the Fairmont Press, Inc., 1996.
- [7] S. Taira et al., "A Method of X-Ray Microbeam Measurement of Local Stress and its Application to Fatigue Crack Growth Problems", J. Mat. Sci. Japan. 27, 1977, p.251-256.
- [8] T. Kondoh et al., "X-Ray Stress Measurement for Titanium Aluminide Intermetallic Compound" Adv. In X-Ray Anal. Vol.43, 2000, p107-116.
- [9] T. Sasaki et al., "Measurement of Macro- and Microstresses of Composite Materials by X-Ray Diffraction Method Using Imaging Plate", ICDD Publications, Vol. 41, 1999, p479-492.

# Residual Stress Field Prediction in Shot Peened Mechanical Parts with Complex Geometries

Maxime Gelineau<sup>1, a\*</sup>, Laurent Barrallier<sup>2, b</sup>, Emmanuelle Rouhaud<sup>3, c</sup>,  
Régis Kubler<sup>2, d</sup> and Quentin Puydt<sup>1, e</sup>

<sup>1</sup>Institut de Recherche Technologique M2P, 4 rue Augustin Fresnel, 57070 Metz – France

<sup>2</sup>Arts et Métiers ParisTech d'Aix-en-Provence, Laboratory of Mechanics Surface and Materials Processing (MSMP), 2 cours des Arts et Métiers, 13617 Aix-en-Provence – France

<sup>3</sup>Université de Technologie de Troyes, Laboratory of Mechanical Systems and concurrent Engineering (LASMIS), 12 rue Marie Curie BP 2060, 10010 Troyes – France

<sup>a</sup>maxime.gelineau@irt-m2p.fr, <sup>b</sup>laurent.barrallier@ensam.eu, <sup>c</sup>emmanuelle.rouhaud@utt.fr,  
<sup>d</sup>regis.kubler@ensam.eu, <sup>e</sup>quentin.puydt@irt-m2p.fr

**Keywords:** Shot Peening, Residual Stresses, Complex Geometries, Finite Element Simulation

**Abstract.** In order to introduce automatically the residual stresses field into a Finite Element model with complex geometry, a PYTHON code has been developed and linked to the software ABAQUS. A comparison between modelling and experiment is carried out by using X-ray diffraction analysis to determine the in-depth residual stress state of Ni-based alloy samples after shot peening.

## Introduction

Most manufacturing industries perform mechanical surface treatments at the end of the manufacturing chain to reinforce relevant working parts. Shot peening is probably the most common of those processes. This treatment modifies the near surface of treated parts by introducing compressive residual stresses due to the repeated impacts of shots leading to an enhanced life.

The objective of this work is to simulate the residual stress state after shot peening, for mechanical parts with complex geometries (thin sheets, curved surfaces). It is part of an industrial collaborative project which one of the work packages consists in developing a complete simulation model of a structure made of a Ni-based alloy and submitted to cyclic loadings in service including the manufacturing process history.

## Numerical Model

**Introducing residual stresses in a Finite Element model.** Several methods have been developed to introduce the stress-free strains into a Finite Element model [1]. Indeed, depending on the capabilities of the finite-element codes, it is possible to introduce the plastic deformation field and/or the stress field as initial conditions. Nevertheless these methods are not directly applicable if the geometry of the part is complex. They require some assumptions:

- The analytical technique used is available only if the geometry of the treated part can be reduced to a semi-infinite body. It means that the treatment is homogeneous, the treated surface is regular and the depth affected by the treatment ( $\Delta$  in Fig. 1) is small (few hundred micrometers) compared to the other dimensions of the part ( $\Delta \ll e$ , e.g. for sheet of thickness  $e$ ).
- The computational technique implies that the geometry has to be plane in order to introduce in a convenient way the mechanical fields into the model.